



<b>Publication Year</b>	2016
<b>Acceptance in OA</b>	2020-10-19T09:35:51Z
<b>Title</b>	ISM Masses and the Star formation Law at $Z = 1$ to 6: ALMA Observations of Dust Continuum in 145 Galaxies in the COSMOS Survey Field
<b>Authors</b>	Scoville, N., Sheth, K., Aussel, H., Vanden Bout, P., Capak, P., BONGIORNO, ANGELA, Casey, C. M., Murchikova, L., Koda, J., Álvarez-Márquez, J., Lee, N., Laigle, C., McCracken, H. J., Ilbert, O., Pope, A., Sanders, D., Chu, J., Toft, S., Ivison, R. J., Manohar, S.
<b>Publisher's version (DOI)</b>	10.3847/0004-637X/820/2/83
<b>Handle</b>	<a href="http://hdl.handle.net/20.500.12386/27879">http://hdl.handle.net/20.500.12386/27879</a>
<b>Journal</b>	THE ASTROPHYSICAL JOURNAL
<b>Volume</b>	820



# ISM MASSES AND THE STAR FORMATION LAW AT $Z = 1$ TO 6: ALMA OBSERVATIONS OF DUST CONTINUUM IN 145 GALAXIES IN THE COSMOS SURVEY FIELD

N. SCOVILLE<sup>1</sup>, K. SHETH<sup>2</sup>, H. AUSSEL<sup>3</sup>, P. VANDEN BOUT<sup>4</sup>, P. CAPAK<sup>5</sup>, A. BONGIORNO<sup>6</sup>, C. M. CASEY<sup>7</sup>, L. MURCHIKOVA<sup>1</sup>, J. KODA<sup>8</sup>, J. ÁLVAREZ-MÁRQUEZ<sup>9</sup>, N. LEE<sup>10</sup>, C. LAIGLE<sup>11</sup>, H. J. MCCRACKEN<sup>11</sup>, O. ILBERT<sup>9</sup>, A. POPE<sup>12</sup>, D. SANDERS<sup>10</sup>, J. CHU<sup>10</sup>, S. TOFT<sup>13</sup>, R. J. IVISON<sup>14,15</sup>, AND S. MANOHAR<sup>1</sup>

<sup>1</sup> California Institute of Technology, MC 249-17, 1200 East California Boulevard, Pasadena, CA 91125, USA

<sup>2</sup> North American ALMA Science Center, National Radio Astronomy Observatory, 520 Edgemont Road, Charlottesville, VA 22901, USA

<sup>3</sup> AIM Unité Mixte de Recherche CEA CNRS, Université Paris VII UMR n158, Paris, France

<sup>4</sup> National Radio Astronomy Observatory, 520 Edgemont Road, Charlottesville, VA 22901, USA

<sup>5</sup> Spitzer Science Center, MS 314-6, California Institute of Technology, Pasadena, CA 91125, USA

<sup>6</sup> INAF—Osservatorio Astronomico di Roma, Via di Frascati 33, I-00040 Monteporzio Catone, Rome, Italy

<sup>7</sup> Department of Astronomy, The University of Texas at Austin, 2515 Speedway Boulevard Stop C1400, Austin, TX 78712, USA

<sup>8</sup> Department of Physics and Astronomy, SUNY Stony Brook, Stony Brook, NY 11794-3800, USA

<sup>9</sup> Laboratoire d’Astrophysique de Marseille (LAM), Université d’Aix-Marseille & CNRS, UMR7326, 38 rue F. Joliot-Curie, F-13388 Marseille Cedex 13, France

<sup>10</sup> Institute for Astronomy, 2680 Woodlawn Drive, University of Hawaii, Honolulu, Hawaii, HI 96822, USA

<sup>11</sup> CNRS, UMR 7095, Institut d’Astrophysique de Paris, F-75014, Paris, France

<sup>12</sup> Department of Astronomy, University of Massachusetts, Amherst, MA 01003, USA

<sup>13</sup> AD, Dark Cosmology Centre, Niels Bohr Institute, University of Copenhagen, Juliana Mariesvej 30, DK-2100 Copenhagen, Denmark

<sup>14</sup> Institute for Astronomy, University of Edinburgh, Blackford Hill, Edinburgh EH9 3HJ, UK

<sup>15</sup> ESO, Karl-Schwarzschild-Strasse 2, D-85748 Garching, Germany

Received 2015 May 7; accepted 2016 February 10; published 2016 March 22

## ABSTRACT

ALMA Cycle 2 observations of long-wavelength dust emission in 145 star-forming galaxies are used to probe the evolution of the star-forming interstellar medium (ISM). We also develop a physical basis and empirical calibration (with 72 low- $z$  and  $z \sim 2$  galaxies) for using the dust continuum as a quantitative probe of ISM masses. The galaxies with the highest star formation rates (SFRs) at  $\langle z \rangle = 2.2$  and 4.4 have gas masses up to 100 times that of the Milky Way and gas mass fractions reaching 50%–80%, i.e., gas masses  $1\text{--}4\times$  their stellar masses. We find a single high- $z$  star formation law:  $\text{SFR} = 35 M_{\text{mol}}^{0.89} \times (1+z)_{z=2}^{0.95} \times (\text{sSFR})_{\text{MS}}^{0.23} M_{\odot} \text{yr}^{-1}$ —an approximately linear dependence on the ISM mass and an increased star formation efficiency per unit gas mass at higher redshift. Galaxies above the main sequence (MS) have larger gas masses but are converting their ISM into stars on a timescale only slightly shorter than those on the MS; thus, these “starbursts” are largely the result of having greatly increased gas masses rather than an increased efficiency of converting gas to stars. At  $z > 1$ , the entire population of star-forming galaxies has  $\sim 2\text{--}5$  times shorter gas depletion times than low- $z$  galaxies. These shorter depletion times indicate a different mode of star formation in the early universe—most likely dynamically driven by compressive, high-dispersion gas motions—a natural consequence of the high gas accretion rates.

*Key words:* cosmology: observations – galaxies: evolution – galaxies: ISM

## 1. INTRODUCTION

For star-forming galaxies, there exists a main sequence (MS) with galaxy star formation rates (SFRs) varying nearly linearly with stellar mass (Noeske et al. 2007). At  $z \sim 2$ , approximately 2% of star-forming galaxies have SFRs more than 4 times higher than the MS, contributing  $\sim 10\%$  of the total star formation (Rodighiero et al. 2011). These galaxies are often identified as the starburst galaxy population (Elbaz et al. 2011; Sargent et al. 2012).

The specific star formation rate ( $\text{sSFR} \equiv \text{SFR}/M_{\text{stellar}}$ ) is roughly constant along the MS at each cosmic epoch but increases 20-fold out to  $z \sim 2.5$ , which is consistent with the overall increase in the cosmic SFR (Hopkins & Beacom 2006; Karim et al. 2011; Whitaker et al. 2012; Lee et al. 2015). Understanding the cause of the MS evolution and the nature of galaxies above the MS is fundamental to understanding the cosmic evolution of star formation.

The interstellar medium (ISM) fuels the activities of both galactic star formation and galactic nuclei—in both cases, peaking at  $z \sim 2$ . Is the cosmic evolution of these activities simply due to galaxies having larger ISM masses ( $M_{\text{ISM}}$ ) at earlier epochs, or are they forming stars with a higher efficiency

( $\epsilon \equiv 1/\tau_{\text{SF}} = \text{SFR}/M_{\text{ISM}}$ )? Specifically, (1) is the 20-fold increase in the SFR of the MS from  $z = 0$  to 2 due to proportionally increased gas contents at early epochs or due to a higher frequency of starburst activity? And (2) are galaxies above the MS converting their gas to stars with higher efficiency or do they simply have more gas than those on the MS? Measurements of the galactic ISM gas content are critical to answering these very basic questions.

Over the last decade, the rotational transitions of CO have been used to probe the molecular ISM of high-redshift galaxies (Solomon & Vanden Bout 2005; Coppin et al. 2009; Tacconi et al. 2010, 2013; Casey et al. 2011; Bothwell et al. 2013; Carilli & Walter 2013). Here, we employ an alternative approach—using the long-wavelength dust continuum to probe ISM masses, specifically, *molecular* ISM masses, at high redshift (Eales et al. 2012; Magdis et al. 2012a; Scoville 2012). This dust emission is optically thin. For high stellar mass star-forming galaxies, the dust continuum can also be detected by ALMA in just a few minutes of observing, whereas for the same galaxies, CO would require an hour or more with ALMA.

Here, we use a sample of 70 galaxies (28 local star-forming galaxies, 12 low-redshift Ultraluminous Infrared Galaxies

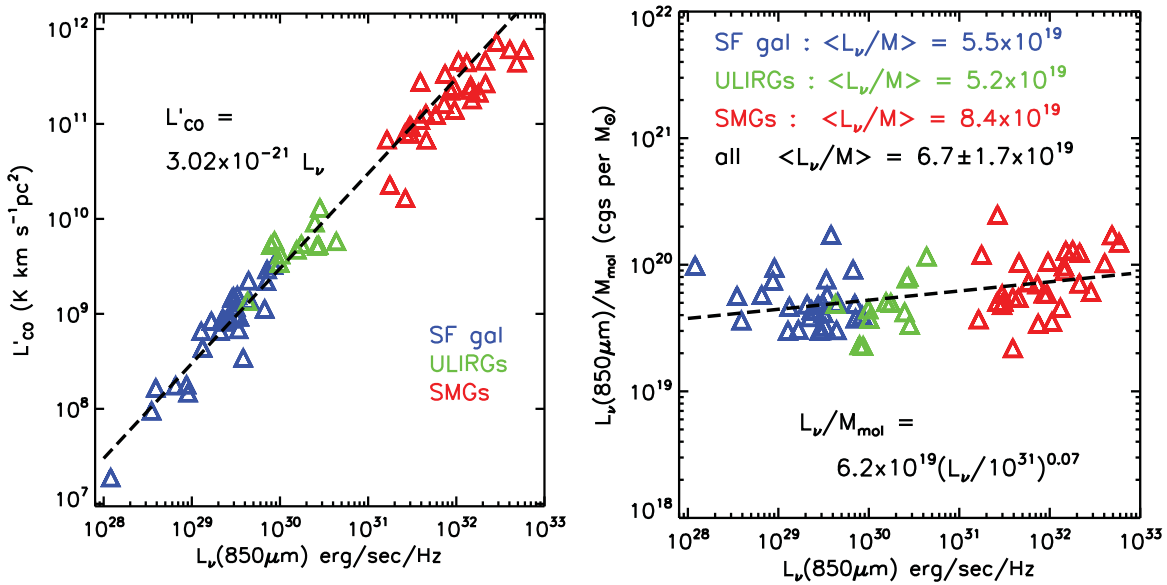


**Figure 1.** Left: the CO(1-0) luminosity and  $L_\nu$  at  $850\ \mu\text{m}$  to  $M_{\text{mol}}$  are shown for three samples of galaxies: normal low- $z$  star-forming galaxies, low- $z$  ULIRGs, and  $z \sim 2$  SMGs. All of the galaxies were selected to have global measurements of CO (1-0) and Rayleigh–Jeans dust continuum fluxes. The large range in apparent luminosities is enhanced by including high-redshift SMGs, many of which in this sample are strongly lensed. Right: the ratio of  $L_\nu$  at  $850\ \mu\text{m}$  to  $M_{\text{mol}}$  is shown for the three samples of galaxies, indicating a very similar proportionality constant between the dust continuum flux and the molecular masses derived from CO(1-0) emission. The molecular masses were estimated from the CO (1-0) luminosities using a single standard Galactic  $X_{\text{CO}} = 3 \times 10^{20}\ \text{N}(\text{H}_2)\ \text{cm}^{-2}\ (\text{K km s}^{-1})^{-1}$  (see Appendix A).

(ULIRGs), and 30 submillimeter galaxies (SMGs) at  $z \sim 2$  to empirically calibrate the ratio of long-wavelength dust emission to CO (1-0) line luminosity, and hence the molecular gas mass. Without making any corrections for variable dust temperatures, galaxy metallicity, or CO excitation variations, the ratio of long-wavelength dust luminosity to CO (1-0) luminosity and molecular gas mass is found to be remarkably constant across this sample, which includes normal star-forming galaxies, starburst galaxies at low redshift, and massive SMGs at  $z = 2\text{--}3$  (see Figure 1).

It is particularly significant that local ULIRGs exhibit the same proportionality between the long-wavelength dust continuum and the CO (1-0) luminosity. (This argues against a different CO-to-H<sub>2</sub> conversion factor in ULIRGs since the physical dependences (on density and  $T_D$  or  $T_K$ ) of the mass to dust and CO emission fluxes are different; this will be discussed in a future work.)

In both the calibration samples and the sample of high-redshift galaxies that we observed with ALMA, we have intentionally restricted the samples to objects with high stellar mass ( $M_{\text{stellar}} = 2 \times 10^{10}\text{--}4 \times 10^{11}\ M_\odot$ ); thus, we are not probing lower metallicity systems where the dust-to-gas abundance ratio is likely to drop or where there could be significant molecular gas without CO (see Bolatto et al. 2013).

The sample of galaxies at high redshift observed with ALMA is described in Section 3. The stellar mass, SFR, submillimeter flux and estimated gas mass for each individual galaxy are tabulated in the tables in Appendix B. The average flux measurements for subsamples of galaxies are presented in Section 4 and the derived gas masses and gas mass fractions in Section 5. Section 6 discusses the variation of ISM mass on and above the main sequence. The implications for the evolution of ISM and star formation at the peak of cosmic activity are discussed in Section 7.

## 2. LONG-WAVELENGTH DUST CONTINUUM AS A GAS MASS TRACER

At long wavelengths, dust emission is optically thin and the observed flux density is proportional to the mass of dust, the dust opacity coefficient, and the mean temperature of dust contributing emission at these wavelengths. Here, we briefly summarize the foundation for using the dust continuum as a quantitative probe of ISM masses; in Appendix A, we provide a thorough description.

To avoid the need to know the dust opacity and the dust-to-gas abundance ratio explicitly, we empirically calibrate the ratio of the specific luminosity at a rest frame of  $850\ \mu\text{m}$  to the ISM molecular gas mass using samples of observed galaxies, thus absorbing the opacity curve, abundance ratio, and dust temperature into a single empirical constant  $\alpha_{850\ \mu\text{m}} = L_{\nu_{850\ \mu\text{m}}}/M_{\text{mol}}$ . This procedure was initially done by Scoville et al. (2013) using three galaxy samples.

In Appendix A, we have redone the calibration of the mass determination from the sub-millimeter-wavelength dust continuum. The sample of calibration galaxies is greatly extended and we use *Herschel* SPIRE  $500\ \mu\text{m}$  imaging instead of SCUBA  $850\ \mu\text{m}$ . The SPIRE observations more accurately recover the extended flux components of nearby galaxies than the SCUBA measurements, which were used in Scoville et al. (2013). (SCUBA observations use beam chopping to remove sky backgrounds, which can compromise the extended flux components.) For the molecular masses, we use CO(1-0) data that is homogeneously calibrated for the local galaxies. The empirical calibration samples now consist of 28 local star-forming galaxies (Table 3), 12 low- $z$  ULIRGs (Table 4), and 30  $z = 1.4\text{--}3$  SMGs (Table 5).

All three samples exhibit the same linear correlation between CO(1-0) luminosity  $L'_{\text{CO}}$  and  $L_{\nu_{850\ \mu\text{m}}}$  as shown in the left panel of Figure 1. To convert the CO luminosities to molecular gas masses, we then use a single CO-to-H<sub>2</sub> conversion constant for all of the objects (Galactic:  $X_{\text{CO}} = 3 \times 10^{20}\ \text{N}(\text{H}_2)\ \text{cm}^{-2}\ (\text{K km s}^{-1})^{-1}$ ) and the resultant masses are shown rated to  $L_{\nu_{850\ \mu\text{m}}}$  in the right

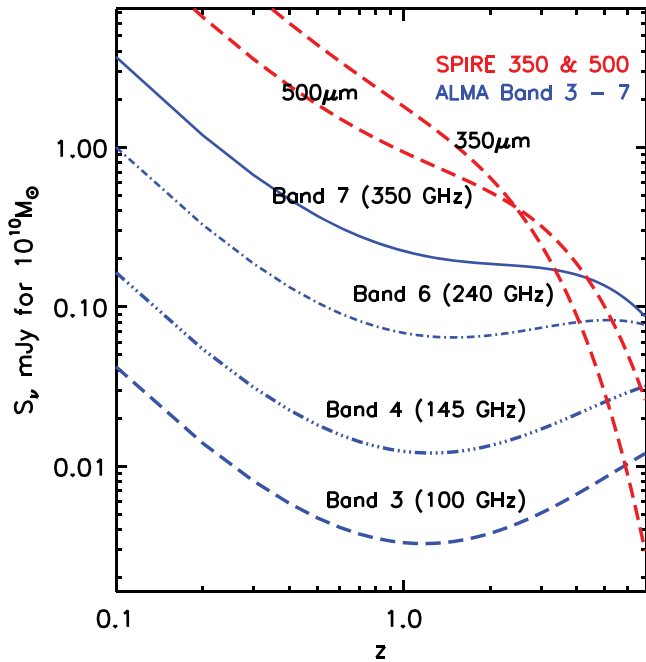


**Figure 2.** Expected continuum fluxes for the ALMA bands at 100, 145, 240, and 350 GHz and for SPIRE 350 and 500  $\mu\text{m}$  for  $M_{\text{mol}} = 10^{10} M_{\odot}$  derived using the empirical calibration embodied in Equation (13), an emissivity power-law index  $\beta = 1.8$ , and including the RJ departure coefficient  $\Gamma_{\text{RJ}}$  (25 K). Since the point-source sensitivities of ALMA in the three bands are quite similar, the optimum strategy is to use Band 7 out to  $z \sim 2$ –3; at higher redshift, lower-frequency ALMA bands are required to avoid large uncertainties in the RJ correction.

panel of Figure 1. We find a single calibration constant  $\alpha_{850 \mu\text{m}} = 6.7 \times 10^{19} \text{ erg s}^{-1} \text{ Hz}^{-1} M_{\odot}^{-1}$  (Equation (13)). (This value for  $\alpha_{850 \mu\text{m}}$  is in excellent agreement with that obtained from Planck data for our Galaxy ( $6.2 \times 10^{19} \text{ erg s}^{-1} \text{ Hz}^{-1} M_{\odot}^{-1}$ , see Appendix A.5). The earlier value used by Scoville et al. (2013) was  $1 \times 10^{20} \text{ erg s}^{-1} \text{ Hz}^{-1} M_{\odot}^{-1}$ .)

The long-wavelength dust emissivity index, which is needed to translate observations at different rest-frame wavelengths, is taken to be  $\beta = 1.8 \pm 0.1$  based on the extensive Planck data in our Galaxy (Planck Collaboration 2011a). The mass of the molecular gas is then derived from the observed flux density using Equation (16), which gives the expected flux density at the observed frequency  $\nu_{\text{obs}}$  for high- $z$  galaxies. Figure 2 shows the expected flux for a fiducial ISM mass of  $10^{10} M_{\odot}$  as a function of redshift for ALMA Bands 3, 4, 6, and 7. These curves can be used to translate our observed fluxes into ISM masses.

### 2.1. Dust Temperatures

Although the sub-millimeter flux will vary linearly with dust temperature (Equation (5)), the range of mass-weighted  $\langle T_D \rangle_M$  will be small, except in very localized regions. For radiatively heated dust,  $T_D$  will vary as the  $1/5$ – $1/6$  power of the ambient radiation energy density, implying a 30-fold increase in the energy density to double the temperature. Extensive surveys of nearby galaxies with *Herschel* find a range of  $T_D \sim 15$ – $30$  K (Dunne et al. 2011; Dale et al. 2012; Auld et al. 2013). Our three calibrations yielding similar values of  $\alpha_{850 \mu\text{m}}$ , including normal star-forming and star bursting systems, lay a solid foundation for using the Rayleigh–Jeans (RJ) dust emission to probe global ISM masses without introducing a variable dust temperature (see Appendix A.2). Here, we advocate the adoption of a single value  $\langle T_D \rangle_M = 25$  K (see Appendix A.2).

In fact, it would be wrong to use a variable temperature correction based on fitting to the overall spectral energy distribution (SED) since the temperature thus derived is a luminosity-weighted  $\langle T_D \rangle_L$ . The difference is easily understood by looking at nearby star-forming giant molecular clouds (GMCs) where spatially resolved far-infrared imaging indicates  $\langle T_D \rangle_L \sim 40$ – $60$  K (dominated by the active star-forming centers), whereas the overall mass-weighted  $\langle T_D \rangle_M \simeq 20$  K (dominated by the more extended cloud envelopes). A good illustration of this might be taken from spatially resolved far-infrared imaging of nearby GMCs. In the Orion, W3, and Auriga GMCs the far-infrared luminosity-weighted dust temperature is  $\sim 50$  K and most of that luminosity originates in the few parsec regions associated with high mass SF (e.g., M42 and the Kleinmann–Low nebula in the case of Orion). On the other hand, most of the cloud mass is in the extended GMC with a 30–40 pc diameter and far-infrared color temperature of  $\sim 15$ – $25$  K (e.g., Motte et al. 2010; Harvey et al. 2013; Rivera-Ingraham et al. 2015).

Within galaxies, there will of course be localized regions where  $T_D$  is significantly elevated—an extreme example is the central 100 pc of Arp 220. There, the dust temperatures reach 100–200 K (Wilson et al. 2014; Scoville et al. 2015); nevertheless, measurements of the whole of Arp 220 are still consistent with the canonical value of  $\alpha_{850 \mu\text{m}}$  adopted here (see Figure 1 in Scoville et al. 2014).

### 3. GALAXY SAMPLES FOR ALMA

Our sample of 145 galaxies is taken from the COSMOS 2  $\text{deg}^2$  survey (Scoville et al. 2007). This survey field has excellent photometric redshifts (Ilbert et al. 2013; Laigle 2016) derived from deep 34-band (UV–Mid IR) photometry. The galaxies were selected to sample stellar masses  $M_{\text{stellar}}$  in the range  $0.2$ – $4 \times 10^{11} M_{\odot}$  and the range of SFRs at each stellar mass. This is not a representative sampling of the galaxy population but is rather meant to cover the range of galaxy properties. Here, 55% of the galaxies are within a factor 2.5 of the SFR on the MS, whereas there is a much larger fraction for the overall population of SF galaxies at  $z \sim 2$ . Forty-eight have spectroscopic redshifts and 120 have at least a single band detection in the infrared with Spitzer MIPS-24  $\mu\text{m}$  or *Herschel* PACS and SPIRE; 65 had 2 or more band detections with *Herschel* PACS/SPIRE.

The photometric redshifts and stellar masses of the galaxies are taken from McCracken et al. (2012), Ilbert et al. (2013), and Laigle (2016). Preference was given to the most recent photometric redshift catalog (Laigle 2016), which makes use of deep Spitzer SPASH IRAC imaging (Steinhardt et al. 2014) and the latest release of COSMOS Ultra-Vista. The SFRs assume a Chabrier stellar initial mass function; they are derived from the rest-frame UV continuum and infrared using *Herschel* PACS and SPIRE data as detailed in Ilbert et al. (2013) and Lee et al. (2015). For sources with detections in at least two of the five available *Herschel* bands,  $L_{\text{IR}}$  is estimated by fitting far-infrared photometry to a coupled, modified graybody plus a mid-infrared power law, as in Casey (2012). The mid-infrared power-law slope and dust emissivity are fixed at  $\alpha = 2.0$  and  $\beta = 1.5$ , respectively.

The original sample of galaxies observed with ALMA had 180 objects. However, subsequent to the ALMA observations, new photometric redshifts (Laigle 2016) and analysis of the *Herschel* PACS and SPIRE measurements in COSMOS (Lee et al. 2015) became available. We have made use of this new ancillary data to refine the sample, including only those objects with the most

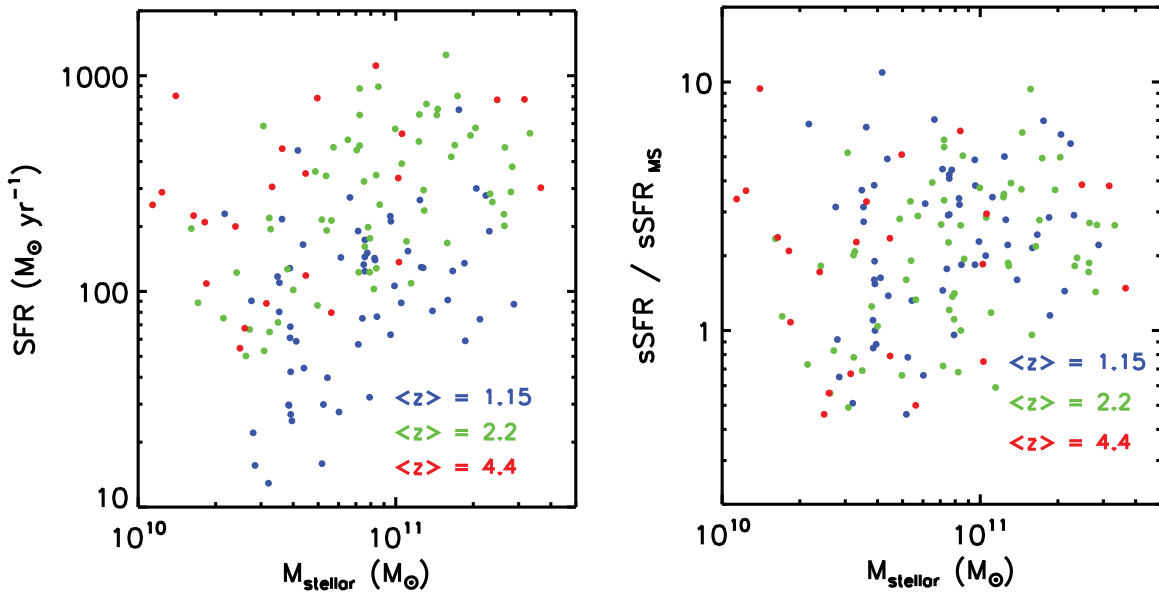


**Figure 3.** Galaxy sample properties. Left: stellar masses and SFRs for the 145 galaxies in our sample—59, 63, and 23 galaxies at each of three redshifts:  $\langle z \rangle = 1.15$ , 2.2, and 4.4. SFRs are the sum of the far-infrared from *Herschel* PACS and SPIRE and the unextincted UV of the galaxy. Right: the galaxies are shown as a function of their specific star formation rates (sSFR) relative to the sSFR of the star-forming main sequence at each galaxy’s redshift and stellar mass. The main-sequence definition is taken from Lee et al. (2015) and Schreiber et al. (2015; see the text). At each redshift, the samples probe the variation in ISM molecular gas as a function of both stellar mass and SFR from the galaxy MS to  $\sim 10$  times above the MS.

reliable redshifts, stellar masses, and SFRs (as judged from the photometric redshift fitting uncertainties). We also required that the derived stellar masses agree within a factor of two between the two most recent photometric redshift catalogs (Ilbert et al. 2013; Laigle 2016). The individual objects are tabulated in Appendix B. There, the adopted redshifts, stellar masses, and SFRs for each of the individual galaxies are tabulated in Tables 6–8.

For each galaxy, we also list the sSFR relative to that of the MS at the same redshift and stellar mass ( $\text{sSFR}_{\text{MS}}/\text{sSFR}_{\text{MS}}$ ). In recent years, there have been numerous works specifying the MS evolution (Noeske et al. 2007; Rodighiero et al. 2011; Béthermin et al. 2012; Speagle et al. 2014; Lee et al. 2015; Schreiber et al. 2015). The last two works have similar specifications for the MS as a function of stellar mass at low redshift. Here, we use Lee et al. (2015) with no evolution of the MS beyond  $z = 2.5$ , i.e.,  $\text{MS}(z > 2.5) = \text{MS}(z = 2.5)$ . The Lee et al. (2015) MS was adopted here since the infrared-based SFRs were also taken from Lee et al. (2015); thus, the SFRs will have the same calibration. The three subsamples with 59, 63, and 23 galaxies at  $\langle z \rangle \sim 1.15$ , 2.2, and 4.4, respectively, probe SFRs from the MS up to  $10 \times \text{sSFR}_{\text{MS}}$  with  $M_{\text{stellar}} = 0.2\text{--}4 \times 10^{11} M_{\odot}$  (Figure 3 and Table 1).

#### 4. OBSERVATIONS AND FLUX MEASUREMENTS

The ALMA Cycle 2 observations (#2013.1.00034.S) were obtained in 2014–2015. The  $z = 1.15$  and 2.2 samples were observed in Band 7 (345 GHz) and the  $z = 4.4$  sample in Band 6 (240 GHz). On-source integration times were  $\sim 2$  minutes per galaxy and average rms sensitivities were 0.152 (Band 7) and 0.065 mJy beam $^{-1}$  (Band 6). Synthesized beam sizes were  $\sim 0''.6\text{--}1''$ . Data were calibrated and imaged with natural weighting using CASA.

The detection rates are summarized in Figure 4 as a function of flux (left panel) and ISM mass (right panel), and in Figure 5 as a function of  $M_{\text{stellar}}$  and sSFR. The detection rates for individual galaxies are  $\sim 70$ , 85, and 50% at  $z = 1.15$ , 2.2, and 4.4, respectively. All of the flux measurements are restricted to

within  $1''.5$  of the galaxy position. For detections, we searched for significant peaks or aperture-integrated flux within the central  $3''$  surrounding each program source. We required a  $2\sigma$  detection in  $S_{\text{tot}}$  or  $3.6\sigma$  in  $S_{\text{peak}}$  in order for the detection to be classified as real. These limits ensure that there would be less than 1 spurious detection in the 145 objects. Noise estimates for the integrated flux measures were derived from the dispersion in the aperture-integrated fluxes for 100 equivalent apertures, displaced off-source in the same image.

#### 5. STACKED SAMPLES

Here, we focus on the results derived from stacking the images of subsamples of galaxies in cells of  $M_{\text{stellar}}$  and sSFR (Figure 5). The galaxy images of all galaxies in each cell were both median- and average-stacked. Given the small numbers of galaxies in many of the subsamples (see Figure 5), we used the average stack rather than the median; for such small samples, the median can have a higher dispersion. Flux and mass measurements for the stacked subsamples of galaxies are given in Table 1 along with the mean sSFR and  $M_{\text{stellar}}$  of each cell.

##### 5.1. Gas Masses

Figure 6 shows the derived mean gas masses and gas mass fractions of each cell for the three redshifts. The values for  $M_{\text{mol}}$  and the gas mass fraction ( $M_{\text{mol}}/(M_{\text{mol}} + M_{\text{stellar}})$ ) are given by the large numbers in each cell and the statistical significance is given by the smaller number in the upper right of each cell.

The top panel of Figure 6 shows a large increase in the ISM masses from  $z = 1.15$  to  $z = 2.2$  for galaxies with stellar mass  $\geq 10^{11} M_{\odot}$  and for galaxies with  $\text{sSFR}/\text{sSFR}_{\text{MS}} \geq 4$  (i.e., galaxies in the upper right of the diagrams). For lower-mass galaxies and galaxies at or below the MS, less evolutionary change is seen, although the MS is itself evolving upwards in sSFR. From  $z = 2.2$  to 4.4, there is milder evolution since approximately equal numbers of cells have higher and lower  $M_{\text{mol}}$  at  $z = 4.4$  compared with  $z = 2.2$  and the differences do not appear to be strongly correlated with sSFR and  $M_{\text{stellar}}$ .

**Table 1**  
Stacked Galaxy Samples

Stack	# Galaxies	$S_{\text{pix}}$ (mJy beam $^{-1}$ )	$S_{\text{total}}$ (mJy)	S/N <sup>a</sup>	$\langle z \rangle$	$\langle M_{*} \rangle$ ( $10^{11} M_{\odot}$ )	$\langle \text{SFR} \rangle$ ( $M_{\odot} \text{ yr}^{-1}$ )	$\langle \text{sSFR} \rangle$ (sSFR <sub>MS</sub> )	$\langle M_{\text{mol}} \rangle$ ( $10^{10} M_{\odot}$ )	$\langle \tau_{\text{SF}} \rangle$ (Gyr)	$M_{\text{mol}} / (M_{*} + M_{\text{mol}})$
$\langle z \rangle = 1.15$											
lowz cell 1	6	0.11 ± 0.05	0.14 ± 0.05	2.96	1.06	0.34	22	0.79	0.66	0.30	0.16 ± 0.054
lowz cell 2	4	0.13 ± 0.07	0.30 ± 0.08	3.96	1.15	0.60	26	0.70	1.41	0.54	0.19 ± 0.048
lowz cell 4	4	0.16 ± 0.08	0.73 ± 0.08	9.20	1.14	0.39	51	1.54	3.43	0.67	0.47 ± 0.051
lowz cell 5	8	0.92 ± 0.17	0.27 ± 0.05	4.99	1.15	0.69	67	1.72	4.34	0.65	0.39 ± 0.070
lowz cell 6	8	0.81 ± 0.12	0.40 ± 0.04	8.98	1.21	1.75	91	1.86	3.93	0.43	0.18 ± 0.027
lowz cell 7	5	0.86 ± 0.16	0.39 ± 0.06	6.47	1.12	0.35	105	3.37	4.07	0.39	0.53 ± 0.101
lowz cell 8	12	1.17 ± 0.14	0.43 ± 0.04	11.26	1.18	0.75	154	3.74	5.61	0.37	0.43 ± 0.052
lowz cell 9	6	1.94 ± 0.23	0.42 ± 0.06	7.47	1.23	1.54	178	3.60	9.46	0.53	0.38 ± 0.046
lowz cell 10	2	0.85 ± 0.34	0.79 ± 0.09	8.96	1.23	0.31	221	6.65	4.17	0.19	0.57 ± 0.230
lowz cell 11	2	2.07 ± 0.20	0.73 ± 0.09	8.19	1.25	0.50	390	9.61	10.06	0.26	0.67 ± 0.063
lowz cell 12	1	2.11 ± 0.50	1.46 ± 0.15	9.64	1.20	2.06	300	6.15	10.19	0.34	0.33 ± 0.079
$\langle z \rangle = 2.2$											
midz cell 1	6	0.15 ± 0.05	0.19 ± 0.06	3.07	2.20	0.28	64	0.67	1.05	0.16	0.27 ± 0.088
midz cell 2	3	0.27 ± 0.08	0.26 ± 0.05	5.41	2.73	0.71	115	0.71	2.26	0.20	0.24 ± 0.074
midz cell 3	2	0.39 ± 0.05	0.31 ± 0.05	5.67	2.66	1.21	117	0.64	3.78	0.32	0.24 ± 0.031
midz cell 4	6	0.38 ± 0.02	0.40 ± 0.04	9.30	2.20	0.28	173	1.82	2.80	0.16	0.50 ± 0.054
midz cell 5	11	0.75 ± 0.11	0.69 ± 0.05	15.24	2.24	0.68	191	1.48	4.09	0.21	0.37 ± 0.056
midz cell 6	9	1.05 ± 0.06	1.22 ± 0.05	26.79	2.25	2.01	266	1.75	6.70	0.25	0.25 ± 0.009
midz cell 7	1	1.66 ± 0.55	0.90 ± 0.15	6.01	2.34	0.31	585	5.19	9.17	0.16	0.75 ± 0.246
midz cell 8	11	0.87 ± 0.03	0.94 ± 0.04	26.12	2.43	0.74	608	4.02	5.90	0.10	0.44 ± 0.017
midz cell 9	12	2.56 ± 0.04	3.06 ± 0.04	70.57	2.30	1.82	559	3.56	16.83	0.30	0.48 ± 0.007
midz cell 12	3	1.79 ± 0.14	2.60 ± 0.08	34.13	1.94	1.60	885	7.56	13.99	0.16	0.47 ± 0.014
$\langle z \rangle = 4.4$											
highz cell 1	3	0.11 ± 0.05	0.15 ± 0.04	3.99	4.71	0.27	70	0.57	1.84	0.26	0.40 ± 0.100
highz cell 2	2	0.08 ± 0.04	0.12 ± 0.04	2.75	4.23	0.51	97	0.63	1.50	0.15	0.23 ± 0.082
highz cell 3	1	0.55 ± 0.11	0.20 ± 0.06	3.54	4.04	1.03	137	0.75	6.90	0.50	0.40 ± 0.078
highz cell 4	5	0.12 ± 0.06	0.10 ± 0.03	3.72	4.63	0.22	211	1.90	1.52	0.07	0.40 ± 0.191
highz cell 5	1	0.13 ± 0.06	0.16 ± 0.06	2.59	5.59	0.45	352	2.35	2.00	0.06	0.31 ± 0.119
highz cell 6	2	1.17 ± 0.26	0.67 ± 0.04	15.59	4.52	2.21	321	1.68	14.33	0.45	0.39 ± 0.088
highz cell 7	3	0.27 ± 0.11	0.15 ± 0.04	4.13	4.25	0.19	328	3.44	3.40	0.10	0.64 ± 0.262
highz cell 8	1	2.24 ± 0.40	1.33 ± 0.06	23.27	3.54	0.50	788	5.10	28.95	0.37	0.85 ± 0.152
highz cell 9	3	1.37 ± 0.08	0.94 ± 0.04	23.98	4.03	2.24	696	3.54	17.16	0.25	0.43 ± 0.025
highz cell 10	1	0.60 ± 0.14	0.24 ± 0.07	3.60	4.18	0.14	807	9.40	7.45	0.09	0.84 ± 0.201
highz cell 11	1	3.84 ± 0.35	2.49 ± 0.06	39.14	4.64	0.84	1114	6.35	47.03	0.42	0.85 ± 0.077

**Notes.**

$\tau_{\text{SF}} = M_{\text{mol}} / \langle \text{SFR} \rangle$  where  $\langle \text{SFR} \rangle$  is the mean SFR.

<sup>a</sup> S/N is the higher of the S/N<sub>tot</sub> and S/N<sub>peak</sub> (see text).

**5.2. Gas Mass Fractions**

The gas mass fractions shown in the bottom panel of Figure 6 range from  $\sim 0.2$ – $0.5$  on the MS (bottom two rows of cells) up to  $0.5$ – $0.8$  for the highest sSFR cells.

For perspective, we note that the Milky Way galaxy has a stellar mass of  $\simeq 6 \times 10^{10} M_{\odot}$  (McMillan 2011),  $M_{\text{ISM}} \sim 3$ – $6 \times 10^9 M_{\odot}$  (approximately equally contributed by H I and H<sub>2</sub>), and SFR  $\sim 1$ – $2 M_{\odot} \text{ yr}^{-1}$ . Thus, for the Galaxy, sSFR  $\simeq 0.015$ – $0.030 \text{ Gyr}^{-1}$  and the gas mass fraction is  $\sim 0.055$ . Finally, to place the Milky Way in context at low  $z$ , the MS parameters given by Béthermin et al. (2012) and Lee et al. (2015) yield SFR = 4.2 and  $3.8 M_{\odot} \text{ yr}^{-1}$  and sSFR = 0.07 and  $0.063 \text{ Gyr}^{-1}$  for the Milky Way’s stellar mass; thus, the Galaxy has a SFR  $\sim 2$  times below the  $z = 0$  MS but is still classified as an MS galaxy.

Compared to the Galaxy, the MS galaxies at  $z = 1$ – $6$  therefore have  $\sim 5$ – $10$  times higher gas mass fractions for the same stellar mass and  $\sim 100$  times higher gas masses in the highest stellar mass

galaxies. At low redshift, such massive galaxies ( $M_{\text{stellar}} = 4 \times 10^{11} M_{\odot}$ ) would have largely evolved to become passive (non-star-forming) red galaxies with much lower ISM masses.

The trends in gas masses, SFRs, and gas mass fractions can be represented adequately by quite simple analytic functions. Using the IDL implementation of the Levenberg–Marquardt algorithm for nonlinear least-squares fitting (LMFIT) of the data shown in Figure 6 and Table 1, we obtain

$$\frac{M_{\text{mol}}}{M_{\text{mol}} + M_{\text{stellar}}} = (0.30 \pm 0.02) \left( \frac{M_{\text{stellar}}}{10^{11} M_{\odot}} \right)^{-0.02 \pm 0.02} \times \left( \frac{1+z}{3} \right)^{0.44 \pm 0.05} \left( \frac{\text{sSFR}}{\text{sSFR}_{\text{MS}}} \right)^{0.32 \pm 0.02} \quad (1)$$

The parameter uncertainties in Equation (1) are those obtained from the Levenberg–Marquardt algorithm. We also attempted

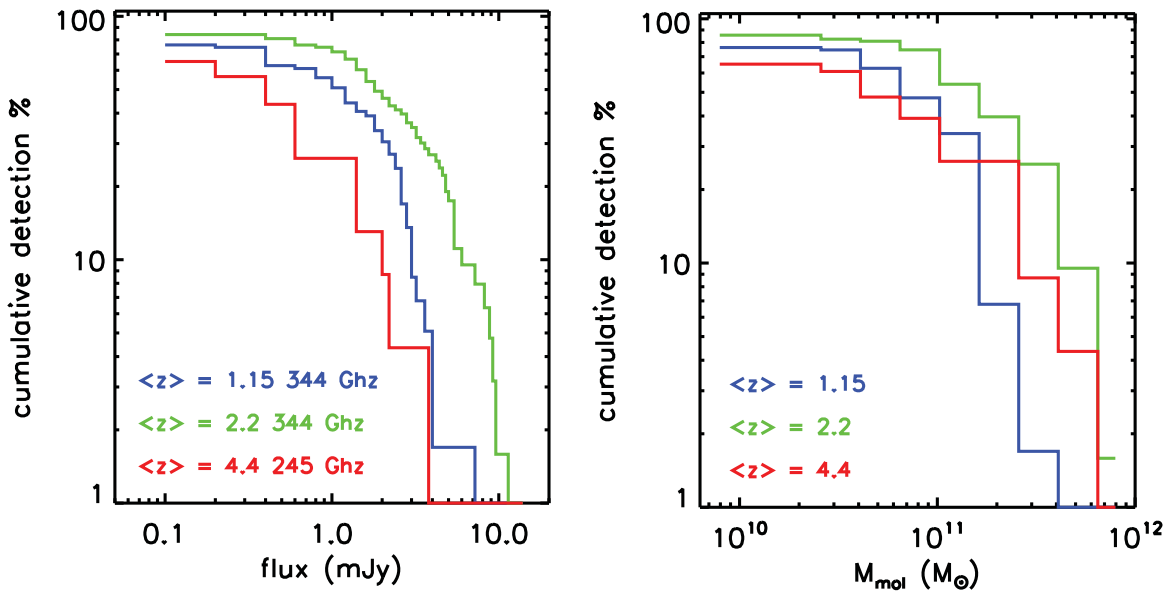


**Figure 4.** Left: the cumulative distribution of detection rates as a function of flux in Band 7 (for  $z \sim 1.15$  and 2.2) and Band 6 (for  $z \sim 4.4$ ). Right: the corresponding detection rates for molecular mass using the flux to mass conversion developed in Appendix A and shown in Figure 2.

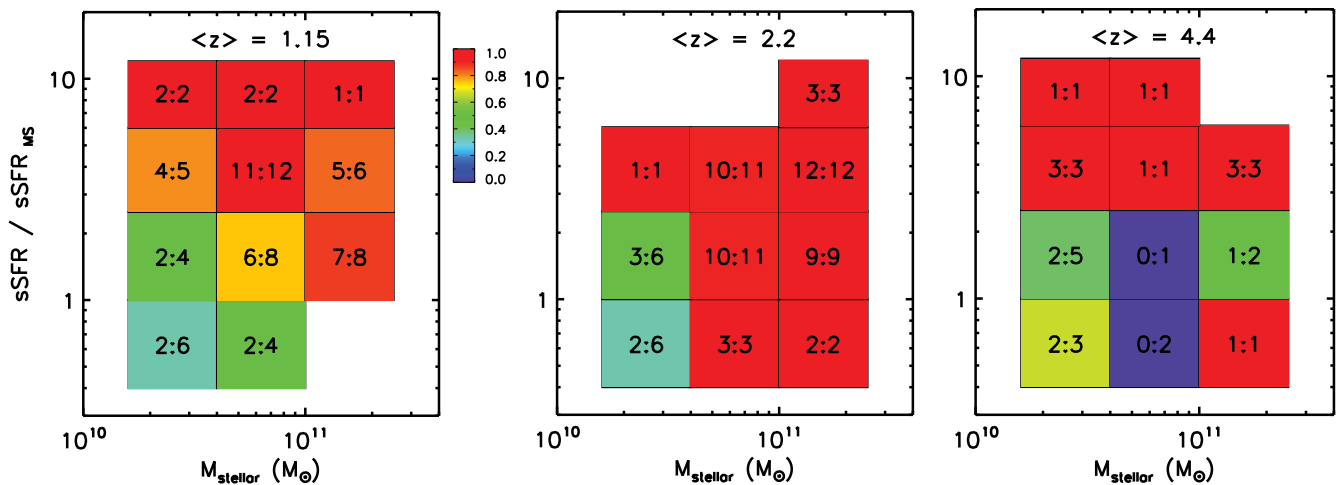


**Figure 5.** Galaxy detection rates as a function of sSFR (relative to the main sequence) and  $M_{\text{stellar}}$  for the three redshift ranges. Each box shows the detection ratio (number of candidates observed: number of detections). For the MS region (lowest 2 rows), 67% of the observed galaxies are detected; for the higher sSFRs (top 2 rows) the detection rate is 95%.

fitting the gas mass fractions with a  $\text{sSFR}/\text{sSFR}_{\text{MS}}$  term; this did not improve the fit and we therefore kept the simpler, unnormalized SFR term. The gas mass fractions predicted by Equation 1 are shown in Figure 7 for comparison with the observed values shown in Figure 6 (bottom).

The gas mass fractions derived here are quite consistent with values derived in a number of other studies from observations of CO (mostly 2–1 and 3–2 line). Tacconi et al. (2010) obtained a range of 0.2–0.5 at  $z \sim 1.1$  and 0.3–0.8 at  $z \sim 2.3$ . Daddi et al. (2010) estimated a gas mass fraction  $\sim 0.6$  for 6 galaxies at  $z = 1.5$  and Magdis et al. (2012b) measured 0.36 in a Lyman break galaxy at  $z = 3.2$ . Later, more extensive studies were conducted by Tacconi et al. (2013) with 52 galaxies and mean gas fractions of 0.33 and 0.47 at  $z \sim 1.2$  and 2.2, respectively, and Santini et al. (2014).

Several cells in the  $\text{sSFR}-M_{\text{stellar}}$  plane have gas mass fractions of 50%–80%, implying gas masses 1–4 times the

stellar masses. These galaxies have the highest sSFRs at  $z = 2.2$  and 4.4. Clearly, such galaxies cannot be made from the merging of two MS galaxies having gas mass fractions  $\sim 40\%$ , since in a merger the resultant gas mass fraction would remain constant or even decrease (if there is significant conversion of gas to stars in a starburst).

These gas-dominated galaxies with very high sSFR galaxies must therefore indicate a different aspect of galaxy evolution—perhaps either nascent galaxies having  $M_{\text{mol}} > M_{\text{stellar}}$  (yet clearly having prior star formation given their large stellar masses and the presence of metal enriched ISM), or galaxies in environments yielding very high IGM accretion rates. These galaxies share the gas-rich properties of the submillimeter galaxies, yet the ones seen here were selected first in the optical-NIR without pre-selection for dust emission. The gas masses of these systems reach  $4 \times 10^{11} M_{\odot}$ ; they are very likely the progenitors of the present epoch massive elliptical galaxies (Toft et al. 2014).

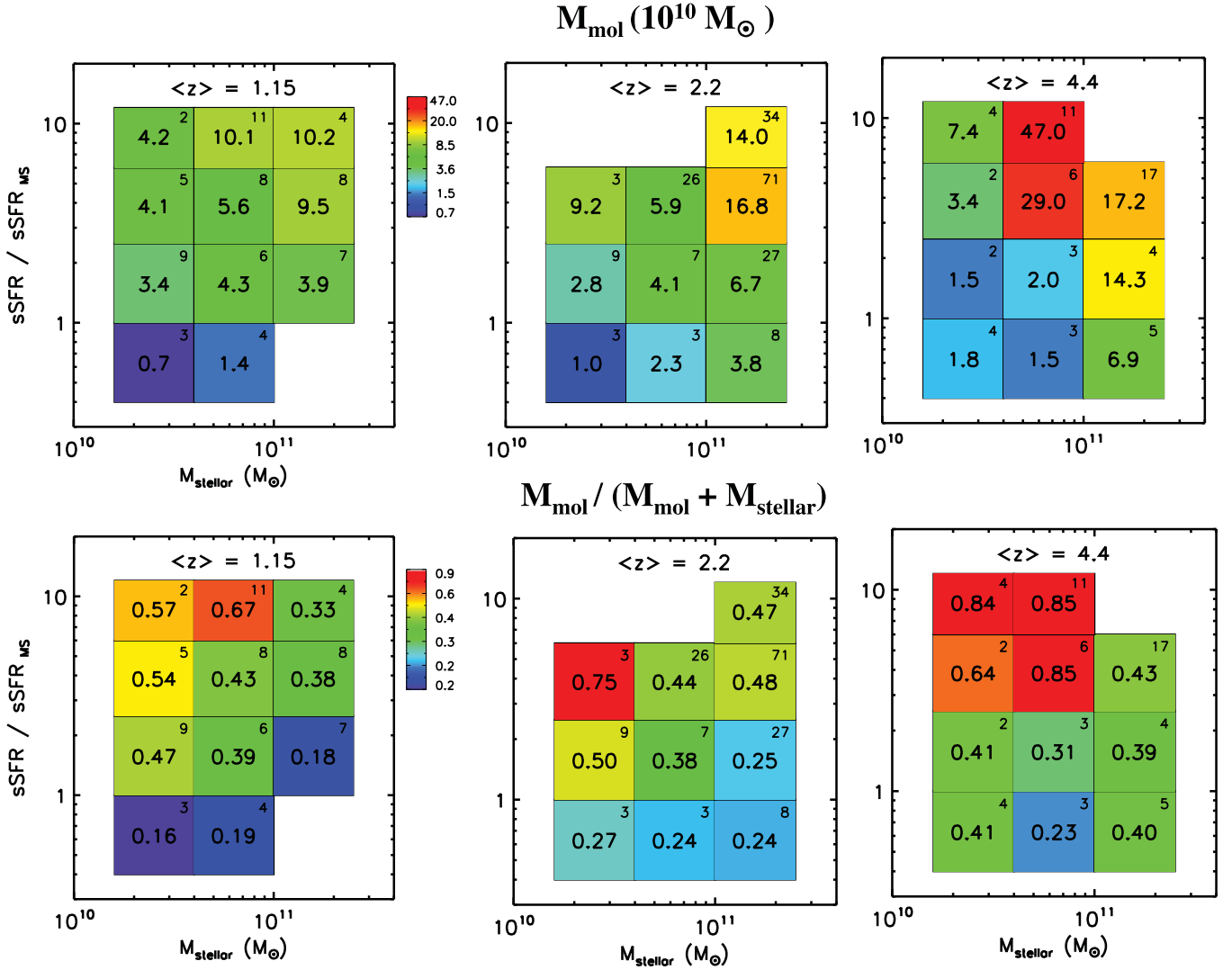


**Figure 6.** Top Row: the gas masses (in units of  $10^{10}M_{\odot}$ ) are shown for the stacked images of galaxy subsamples within each cell of  $M_{\text{stellar}}$  and sSFR (Table 1). The number in the upper right of each cell is the statistical significance or signal-to-noise ratio ( $n\sigma$ ) of the estimate. The ISM masses increase strongly to higher redshift and in galaxies with the highest sSFR. Bottom Row: the gas mass fractions ( $M_{\text{mol}} / (M_{\text{mol}} + M_{\text{stellar}})$ ).

### 5.3. Star Formation Law at High Redshift

Using measurements from the stacking in cells of sSFR and  $M_{\text{stellar}}$  (Table 1 and Figure 8), we obtained a least-squares fit for the SFR dependence on gas mass, redshift, and elevation above the MS:

$$\text{SFR} = (35 \pm 16) \left( \frac{M_{\text{mol}}}{10^{10} M_{\odot}} \right)^{0.89 \pm 0.12} \times \left( \frac{1+z}{3} \right)^{0.95 \pm 0.28} \left( \frac{\text{sSFR}}{\text{sSFR}_{\text{MS}}} \right)^{0.23 \pm 0.15} M_{\odot} \text{ yr}^{-1}. \quad (2)$$

The parameter uncertainties were obtained from the Levenberg–Marquardt procedure.

Equation (2) indicates a high-redshift SF law with an approximately linear dependence on gas mass and an increasing SF efficiency (SFR per unit gas mass) at higher redshift. The dependence on sSFR relative to that on the MS is relatively weak (0.23 power; see also Section 6). No significant dependence (less than  $1\sigma$ ) on stellar mass was found so we omitted the stellar mass term from the fitting for Equation (2).

Inversion of Equation (2) yields an expression for the gas mass in terms of the observed SFRs.

For low-redshift galaxies, Leroy et al. (2013) derive a very similar power-law index (0.95–1) for SF as a function of molecular gas mass but with a lower SF rate per unit ISM mass; this result was also seen in earlier surveys of nearby galaxies in CO (see Young & Scoville 1991).

In Figure 9, we compare the SF law given in Equation (2) with the stacking results of Béthermin et al. (2015) and Álvarez-Márquez et al. (2015). Their 1.1 mm stacked fluxes were translated into gas masses using the procedure developed here in Appendix A. Béthermin et al. (2015) had samples of galaxies at  $z > 1$  both on the MS and at higher SFRs; the Álvarez-Márquez et al. (2015) sample has Lyman Break galaxies at  $z \sim 3$ , presumably mostly MS galaxies. The 1.1 mm measurements on which the mass estimates in Figure 9 are based used very large beams and therefore had many sources within the beam; this confusion was removed statistically (see Béthermin et al. 2015; Álvarez-Márquez et al. 2015). (We do not use their SPIRE 500  $\mu\text{m}$  stacked fluxes since for most of these redshifts  $\lambda_{\text{rest}}$  will be less than 250  $\mu\text{m}$ , and thus are not

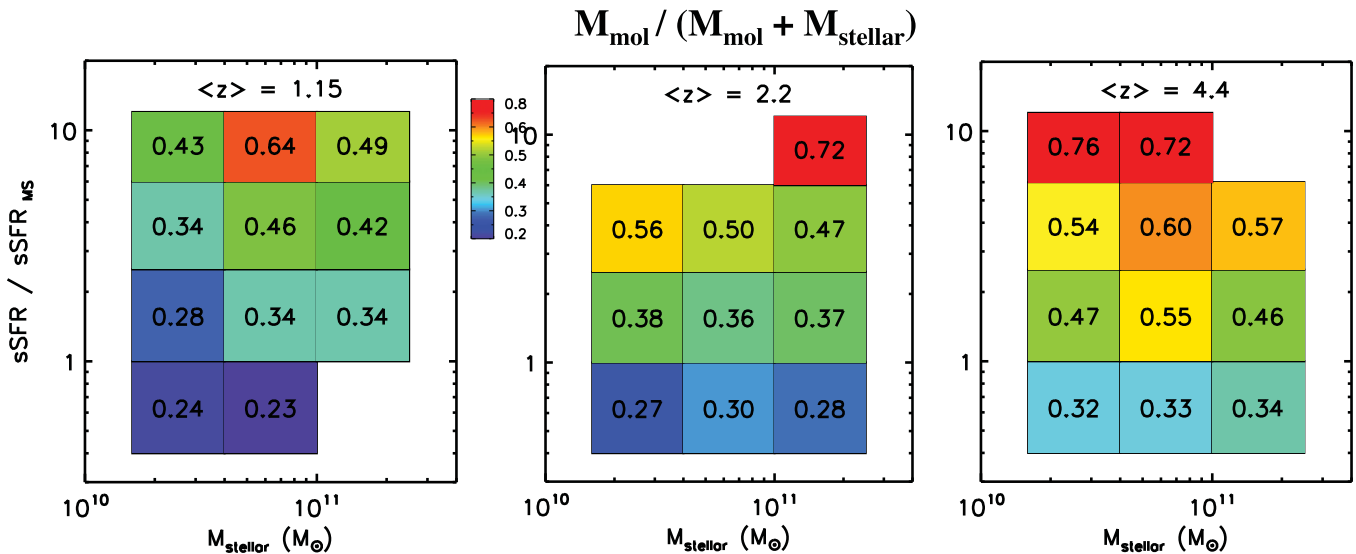


**Figure 7.** Similar to Figure 6 (bottom panel), except that here we show the values obtained from Equation (1) for the same  $M_{\text{stellar}}$  and  $s\text{SFR}$  as the observed cells in Figure 6. The simple analytic fit in Equation (1) adequately describes the trends in the observed cells as a function of SFR,  $M_{\text{stellar}}$ , and redshift.

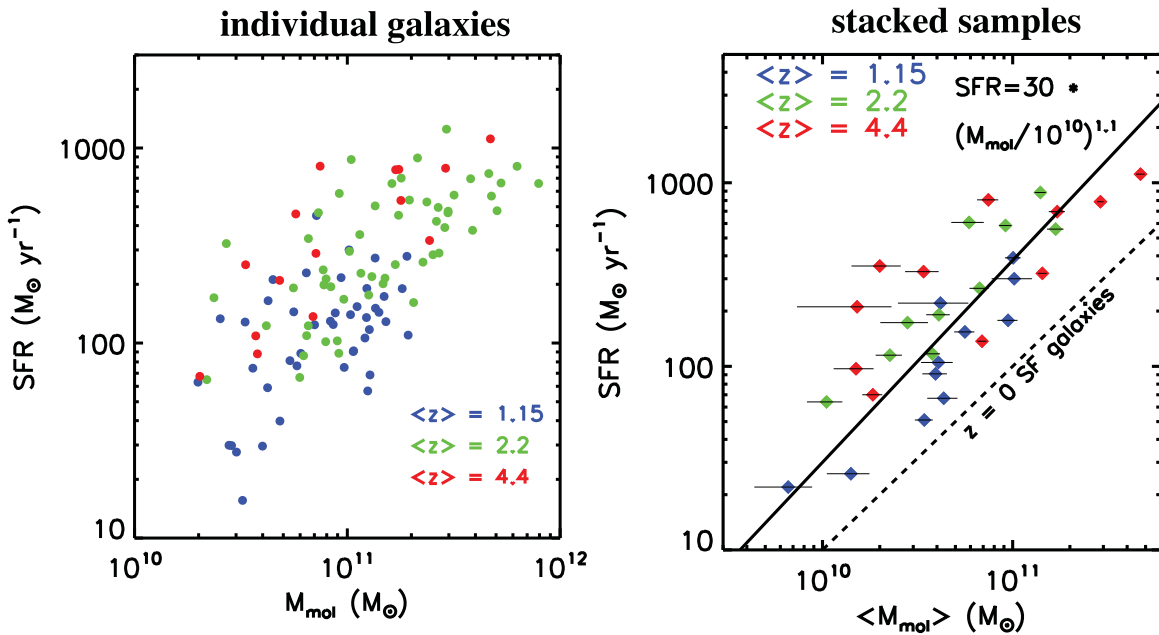


**Figure 8.** Left: the SFRs as a function of  $M_{\text{mol}}$  are shown for the individual galaxies. Right: same as on the left, but for the stacked galaxy samples. The best-fit SF law, given by Equation (2) and evaluated at  $z = 2$ , is shown in the right panel.

safely on the RJ tail.) Figure 9 indicates reasonable agreement between the ALMA results presented here and the 1.1 mm stacking results; both show an approximately linear dependence of the SFRs on the estimated gas masses.

#### 5.4. Gas Depletion Times

The existence of a single “linear” relation between the available gas mass and the SFR for all our galaxies (independent of redshift at  $z > 1$ , both on and above the MS) is a result with fundamental implications. The characteristic ISM depletion time of  $\tau = M_{\text{mol}}/\text{SFR} \simeq 2\text{--}7 \times 10^8$  years (Figure 10) is approximately constant for galaxies both on and above the MS. These are broadly consistent with previously determined typical values. Tacconi et al. (2013) found a mean

gas depletion time of  $\sim 7 \times 10^8$  years for a sample of 53 galaxies with CO at  $z = 1$  to 2.5 and Santini et al. (2014) found  $\sim 1\text{--}3 \times 10^8$  years for a large sample using dust continuum measurements from *Herschel* (see their Figure 7).

The gas depletion time determined here does show evolution with redshift, having shorter timescales at  $z = 2.2$  and shorter still at  $z = 4.4$  compared to  $z = 1.1$ . This timescale is short compared with the  $\sim 2$  Gyr time differences between  $z = 4.4$  and 2.2 and  $z = 2.2$  to 1.15, implying that there must be substantial accretion of fresh gas to replace that being absorbed into stars.

For the nearby galaxies, the gas depletion times are  $\sim 1.5$  Gyr (Young & Scoville 1991; Young et al. 1995; Leroy et al. 2013). The shorter depletion times at high redshift and the universality of these short timescales imply that star formation in the early

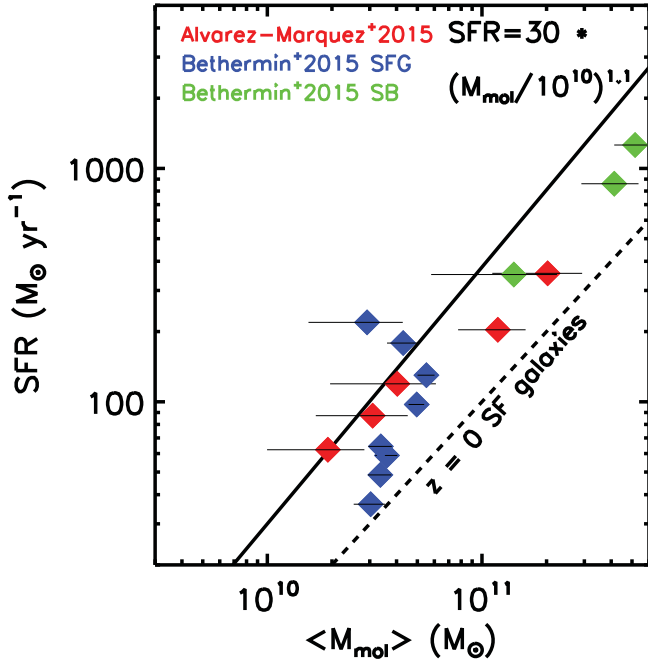


**Figure 9.** Best-fit SF law given by Equation (2) (evaluated for  $z = 2$ ) is compared with the stacking results from Álvarez-Márquez et al. (2015, pp. 142–147) and Béthermin et al. (2015), indicating reasonably good agreement considering the very different approaches. Álvarez-Márquez et al. (2015, pp. 142–147) and Béthermin et al. (2015) did stacking of very large samples of galaxies using *Herschel* SPIRE 350 and 500  $\mu\text{m}$  and Aztec 1.1 mm imaging. Here, we make use of only their 1.1 mm stack fluxes in order to stay on the RJ tail and convert those fluxes to an implied ISM molecular mass using the identical procedure developed here for translating sub-millimeter flux density into mass.

universe is driven by very different processes than those in present day galaxies that have low star formation efficiencies. This different star formation mode, dominant in high-redshift, gas-rich galaxies, is quite plausibly the same dynamically driven SF occurring in low- $z$  galactic spiral arms, bars, and merging systems. However, at high redshift, the higher SF efficiencies occur throughout the SF galaxy population. At high redshift, dispersive gas motions (as opposed to ordered rotation) and/or galaxy interactions will lead to compression in the highly dissipative ISM, enhancing the SFR per unit gas mass. Clearly, such motions will be damped on a galaxy crossing timescale ( $\sim 2 \times 10^8$  years), but this is also the timescale that is implied for the replenishment of the high- $z$  gas masses in order to maintain the observed SFRs. The accreted gas from the intergalactic medium or galaxy merging should have typical infall/free-fall velocities of a few  $\times 100 \text{ km s}^{-1}$ ; i.e., sufficient to maintain the dispersive ISM velocities which then can drive the higher SFRs, elevated relative to  $z = 0$  quiescent galaxies.

## 6. ON VERSUS ABOVE THE MS

In Table 2, we include average properties and gas masses for samples of galaxies on and above the MS for the three redshift ranges. At all three redshifts, the rate of SF per unit gas mass is similar for the MS galaxies and for galaxies with sSFR greater than 2.5 times above the MS (last column in Table 2). In the samples above the MS, the sSFRs are typically 3–4 times above the MS samples, yet the gas depletion times are less than a factor of 2 different. Also, for the complete sample at all

**Table 2**  
Averages for Samples on and above MS

Sample	# Gal.	$\langle z \rangle$	$\langle M_* \rangle$ ( $10^{11} M_\odot$ )	$\langle \text{SFR} \rangle$ ( $M_\odot \text{ yr}^{-1}$ )	$\langle \text{sSFR} \rangle$ /sSFR <sub>MS</sub>	$\langle M_{\text{mol}} \rangle$ ( $10^{10} M_\odot$ )	$\langle f_{\text{mol}} \rangle$	$\langle M_{\text{mol}}/\text{SFR} \rangle$ (Gyr)
$\langle z \rangle = 1.1$								
MS	19	1.16	0.92	64.20	1.48	$6.3 \pm 0.8$	$0.42 \pm 0.04$	$1.09 \pm 0.13$
above MS	25	1.20	0.81	169.15	4.49	$10.6 \pm 0.9$	$0.55 \pm 0.04$	$0.65 \pm 0.07$
all	44	1.19	0.88	123.69	3.15	$9.0 \pm 0.7$	$0.50 \pm 0.03$	$0.84 \pm 0.07$
$\langle z \rangle = 2.2$								
MS	29	2.24	0.99	181.86	1.46	$10.8 \pm 1.3$	$0.52 \pm 0.03$	$0.61 \pm 0.05$
above MS	26	2.28	1.25	571.21	4.24	$29.3 \pm 3.3$	$0.67 \pm 0.02$	$0.51 \pm 0.05$
all	55	2.27	1.15	367.32	2.75	$19.5 \pm 2.2$	$0.59 \pm 0.02$	$0.56 \pm 0.04$
$\langle z \rangle = 4.4$								
MS	6	4.28	0.35	117.36	1.19	$4.3 \pm 0.6$	$0.58 \pm 0.05$	$0.42 \pm 0.04$
above MS	9	4.07	0.66	583.19	4.59	$13.4 \pm 2.4$	$0.68 \pm 0.06$	$0.24 \pm 0.03$
all	15	4.20	0.60	399.54	3.55	$10.6 \pm 2.2$	$0.64 \pm 0.04$	$0.31 \pm 0.04$
all $z$								
MS	54	2.07	0.94	138.43	1.46	$8.8 \pm 0.8$	$0.49 \pm 0.02$	$0.76 \pm 0.05$
above MS	60	2.10	1.06	422.55	4.30	$18.9 \pm 2.3$	$0.62 \pm 0.02$	$0.53 \pm 0.04$
all	114	2.10	1.02	288.46	2.98	$14.2 \pm 1.3$	$0.56 \pm 0.02$	$0.64 \pm 0.04$

**Note.** Samples include all galaxies with  $M_{\text{mol}} > 10^{10} M_\odot$ . Uncertainties in estimates of the means and the ratios were derived from bootstrap resampling of the data samples.

redshifts (last three rows in Table 2), the depletion times differ by only  $\sim 20\%$ .

Comparing the gas masses and depletion times on and above the MS in Table 2, it is clear that the higher SFRs for galaxies with elevated sSFRs are mostly due to those galaxies having much higher gas masses, rather than an increased efficiency, or rate of converting gas to stars. This conclusion is substantiated by fitting function results (Equation (2)), giving a power-law dependence of 0.89 on the gas mass and only 0.23 on the sSFR relative to the MS. Thus, the so-called starburst population is largely a population of very gas-rich galaxies rather than galaxies converting gas to stars more efficiently. In fact, Magdis et al. (2012a) similarly find that the vertical spread of the MS band is due to variations in the gas mass fraction rather than variations in the SF efficiency (see their Section 6.3). On the other hand, Silverman et al. (2015) reach a different conclusion with CO (2-1) observations for seven  $z = 1.6$  galaxies having sSFRs approximately 4 times above the MS. They attribute their lower CO to far-infrared luminosity ratios to a higher star formation efficiency relative to galaxies on the MS. However, the offset shown in their Figure 3(a) is really very small—less than a 30% departure from the CO/FIR ratios occurring on the MS.

## 7. SUMMARY AND COMMENTS

We have provided a thorough physical and empirical foundation for the use of sub-millimeter flux measurements as a probe of the ISM gas mass in galaxies (Appendix A). We find that a single empirical scaling exists between the specific luminosity of the RJ dust continuum ( $L_{\nu_{850\ \mu\text{m}}}$ ) and the mass as determined from CO(1-0) measurements over three orders of magnitude in  $L_{\nu_{850\ \mu\text{m}}}$  (see Figure 1).<sup>16</sup>

The ALMA Band 6 and 7 observations, with typically only a few minutes of integration, detect a majority (79%) of the 145 galaxies in our sample at  $z = 1-6$  (see Figures 4 and 5). Thus, with ALMA, this technique immediately enables surveys of large numbers of objects. Using the RJ dust continuum, one also avoids the uncertainties of CO excitation variations which enter when translating higher rotational line measurements into equivalent CO(1-0) line luminosities, and hence molecular gas masses.

The appropriate temperature characterizing the RJ dust emission is a mass-weighted  $T_d$  and, from a basic understanding of the dust emission, it is clear that a luminosity-weighted  $T_D$  determined from SED fitting in each individual source should not be used in this technique; rather, it is more appropriate to simply adopt a constant value with  $T_D \simeq 25$  K as is done here. This statement applies to global measurements of the dust continuum, not instances where small regions of a galaxy are resolved and have locally enhanced mass-weighted  $T_D$  (e.g., the compact nuclei in Arp 220; Scoville et al. 2015). The galaxies used in our empirical calibration and those observed by us using ALMA are all fairly massive ( $M_{\text{stellar}} > 2 \times 10^{10} M_{\odot}$ ), and so we are not exploring low-metallicity systems where the calibration may depart from constancy due to variations in the dust-to-gas abundance ratio or the dust properties.

The results presented here suggest the following.

1. At high redshift, the primary difference between galaxies with sSFR above the MS and those on the MS is simply the increased gas content of the former, not higher efficiency for conversion of gas to stars.
2. However, the shorter ( $\sim 5\times$ ) gas depletion times at high redshift for all star-forming galaxies, both on and above the MS, imply a more efficient mode for star formation from existing gas supplies. This is naturally a result of highly dispersive gas motions (due to the prodigious on-going accretion needed to replenish gas content and also due to galaxy interactions) for all high-redshift galaxies—those on and above the MS.

Our result of a single SF law at high redshift is very different from some prior studies. Daddi et al. (2010) and Genzel et al. (2010) obtain different SF laws for normal SF galaxies and starburst/SMG galaxies; however, in both cases, their ISM masses at high redshift are derived from higher- $J$  CO transitions and they use different high- $J$  to  $J = 0$  line ratios and CO-to- $\text{H}_2$  conversion factors for the two classes of galaxies (see also Sargent et al. 2014). Genzel et al. (2015) compared CO and dust continuum results in order to constrain the variations in the conversion factor between the MS and starburst population, obtaining general agreement with their earlier results. That their SF laws differ for normal and starburst/SMG galaxies is a result of their use of different CO-to- $\text{H}_2$  conversion factors, which we argue is inappropriate for global ISM measures (Appendix A). The technique we developed here avoids the additional uncertainty introduced when observing higher- $J$  CO transitions at high redshift, and global variations in the mass-weighted  $T_D$  are likely to be small.

We thank Zara Scoville for proof reading the manuscript and Sue Madden for suggesting use of the SPIRE fluxes for calibration. This paper makes use of the following ALMA data: ADS/JAO.ALMA# 2013.1.00034.S. This paper makes use of the following ALMA data: ADS/JAO.ALMA#2013.1.00111.S. ALMA is a partnership of ESO (representing its member states), NSF (USA), and NINS (Japan), together with NRC (Canada), NSC and ASIAA (Taiwan), and KASI (Republic of Korea), in cooperation with the Republic of Chile. The Joint ALMA Observatory is operated by ESO, AUI/NRAO, and NAOJ. The National Radio Astronomy Observatory is a facility of the National Science Foundation operated under cooperative agreement by Associated Universities, Inc. R.J.I. acknowledges support from ERC in the form of the Advanced Investigator Programme, 321302, COSMICISM.

## APPENDIX A LONG WAVELENGTH DUST CONTINUUM AS AN ISM MASS TRACER

Here, we summarize the physical and empirical basis for using long-wavelength dust emission as a probe of ISM mass. The empirical calibration is obtained from: (1) a sample of 30 local star-forming galaxies; (2) 12 low- $z$  ULIRGs; and (3) 30  $z \sim 2$  SMGs. We have completely redone the analysis of these three galaxy samples. We use *Herschel* SPIRE 350 and 500  $\mu\text{m}$  data which provide more reliable total sub-millimeter fluxes for the extended objects at low redshift than were available from the SCUBA 850  $\mu\text{m}$  observations used in Scoville et al. (2014).

<sup>16</sup> The SMG galaxies are probably gravitationally lensed so we do not include their luminosities in this estimate of the dynamic range.

The major differences, compared to the empirical calibration presented in Scoville et al. (2014), are that here we empirically calibrate the sub-millimeter fluxes relative to the molecular gas masses rather than H I plus H<sub>2</sub> (since H I is not well measured in many ULIRGs and not at all in the  $z = 2$  SMGs). We also go back to the original sources for the CO (1-0) luminosities and use a single CO-to-H<sub>2</sub> conversion factor for all of the objects; we expand the samples when we find additional global CO and SPIRE flux measurements and we remove a couple objects where we find errors from the SINGS/KINGFISH surveys (Draine et al. 2007). All of these calibrations yield a very similar rest-frame 850  $\mu\text{m}$  luminosity per unit molecular gas mass with small dispersions. The mean value is also within 10% of the value obtained by Planck for Milky Way molecular gas.

### A.1. Rayleigh–Jeans Dust Continuum—Analytics

The far-infrared-sub-millimeter emission from galaxies is dominated by dust re-emission of the luminosity from stars and active galactic nuclei (AGNs). The luminosity at the peak of the FIR is often used to estimate the luminosity of obscured star formation or AGNs. Equally important (but not often stressed) is the fact that the long-wavelength RJ tail of dust emission is nearly always optically thin, thus providing a direct probe of the total dust, and hence the ISM mass—provided that the dust emissivity per unit mass and the dust-to-gas abundance ratio can be constrained. Here, we take the approach of empirically calibrating the appropriate combination of these quantities rather than requiring determination of each one independently.

The observed flux density from a source at luminosity distance  $d_L$  is

$$S_{\nu_{\text{obs}}} = \frac{(1 - e^{-\tau_d(\nu_{\text{rest}})}) B_{\nu_{\text{rest}}}(T_d)(1 + z)}{d_L^2}, \quad (3)$$

where  $B_{\nu_{\text{rest}}}$  is the Planck function in the rest frame and  $\tau_d(\nu)$  is the source optical depth at the emitted frequency. (The factor  $1 + z$  accounts for the compression of frequency space in the observer’s frame if the source is at significant redshift.) The source optical depth is given by  $\tau_d(\nu) = \kappa(\nu) \times 1.36 N_{\text{H}} m_{\text{H}} = \kappa(\nu) \times M_{\text{gas}}$ , where  $\kappa(\nu)$  is the absorption coefficient of the dust per unit *total mass of gas* (i.e., the effective area per unit mass of gas),  $N_{\text{H}}$  is the column density of H nuclei, and the factor of 1.36 accounts for the mass contribution of heavier atoms (mostly He at 8% by number). Often the dust opacity coefficient is specified per unit mass of dust. However, here we are empirically calibrating the dust opacity relative to the ISM molecular gas mass, and so it is convenient to use the above definition, avoiding a separate specification of the dust opacity coefficient per mass of dust and the dust-to-gas ratio.

At long wavelengths where the dust is optically thin, the flux density is then

$$S_{\nu_{\text{obs}}} = \frac{M_{\text{mol}} \kappa(\nu_{\text{rest}}) B_{\nu_{\text{rest}}}(1 + z)}{d_L^2}. \quad (4)$$

Because  $\kappa$  is per unit gas mass, the gas-to-dust ratio is absorbed in  $\kappa$  and it therefore does not appear explicitly in Equation (4). Written with a Rayleigh–Jeans  $\nu^2$  dependence, as is appropriate

at long wavelengths, Equation (4) becomes

$$S_{\nu_{\text{obs}}} = \frac{M_{\text{mol}} \kappa(\nu_{\text{rest}}) 2kT_d (\nu_{\text{rest}}/c)^2 \Gamma_{\text{RJ}}(T_d, \nu_{\text{obs}}, z)(1 + z)}{d_L^2}, \quad (5)$$

where  $\Gamma_{\text{RJ}}$  is the correction for departure in the rest frame of the Planck function from Rayleigh–Jeans (i.e.,  $B_{\nu_{\text{rest}}}/\text{RJ}_{\nu_{\text{rest}}}$ ).  $\Gamma_{\text{RJ}}$  is given by

$$\Gamma_{\text{RJ}}(T_d, \nu_{\text{obs}}, z) = \frac{h\nu_{\text{obs}}(1 + z)/kT_d}{e^{h\nu_{\text{obs}}(1 + z)/kT_d} - 1}. \quad (6)$$

Equation (5) can be rewritten for the specific luminosity ( $L_{\nu_{\text{rest}}}$ ) in the rest frame of the galaxy:

$$\begin{aligned} L_{\nu_{\text{rest}}} &= S_{\nu_{\text{obs}}} 4\pi d_L^2 / (1 + z) \\ &= \kappa(\nu_{\text{rest}}) 8\pi k T_d (\nu_{\text{rest}}/c)^2 \Gamma_{\text{RJ}} M_{\text{mol}}. \end{aligned} \quad (7)$$

The long-wavelength dust opacity can be approximated by a power law in wavelength:

$$\kappa(\nu) = \kappa(\nu_{850 \mu\text{m}}) (\lambda/850 \mu\text{m})^{-\beta}. \quad (8)$$

We adopt  $\lambda = 850 \mu\text{m}$  ( $\nu = 353 \text{ GHz}$ ) as the fiducial wavelength since it corresponds to most of the high- $z$  SCUBA observations and is the optimum for ALMA (i.e., Band 7). We will use a spectral index of  $\beta \simeq 1.8$  (see Appendix A.3).

The rest-frame luminosity-to-mass ratio at the fiducial wavelength is given by

$$\begin{aligned} \frac{L_{\nu_{850 \mu\text{m}}}}{M_{\text{mol}}} &= \kappa(\nu_{850 \mu\text{m}}) \frac{8\pi k \nu^2}{c^2} T_d \Gamma_{\text{RJ}} \text{ and we define} \\ \alpha_{\nu_{850 \mu\text{m}}} &\equiv \frac{L_{\nu_{850 \mu\text{m}}}}{M_{\text{mol}}} = \frac{8\pi k \nu^2}{c^2} \kappa(\nu_{850 \mu\text{m}}) T_d \Gamma_{\text{RJ}}. \end{aligned} \quad (9)$$

In Appendix A.4, we show that this luminosity-to-mass ratio ( $\alpha_{\nu_{850 \mu\text{m}}}$ ) is relatively constant under a wide range of conditions in normal star-forming and starburst galaxies and at both low and high redshift. Then, once this constant is empirically calibrated, we use measurements of the RJ flux density, and hence the luminosity, to estimate gas masses. We note that this result is equivalent to a constant molecular gas mass to dust mass ratio over a wide range of redshifts for high stellar mass galaxies.

### A.2. Mass-weighted $T_d$

It is important to recognize that the dust temperature relevant to the RJ emission tail is a mass-weighted  $\langle T_d \rangle_M$ . This is definitely not the same as the luminosity-weighted  $\langle T_d \rangle_L$ , which might be derived by fitting the IR SED (determined largely by the wavelength of peak IR emission). The former is a linear weighting with  $T_d$  and the latter is weighted as  $\sim T^{5-6}$  depending on  $\beta$ . In dust clouds with temperature gradients, these temperatures are likely to differ by a factor of a few (depending on the optical depths and mass distributions).

In local star-forming galaxies, the mass-weighted  $\langle T_d \rangle_M \sim 15\text{--}35\text{ K}$ , and even in the most vigorous starbursts like Arp 220, the mass-weighted dust temperature is probably less than 45 K if one considers the entire galaxy; in contrast, the luminosity-weighted  $\langle T_d \rangle_L \sim 50\text{--}200 \text{ K}$  for Arp 220, depending on the size of the region. Therefore, it is incorrect to do an SED fit and use the derived temperature for estimation of the masses.

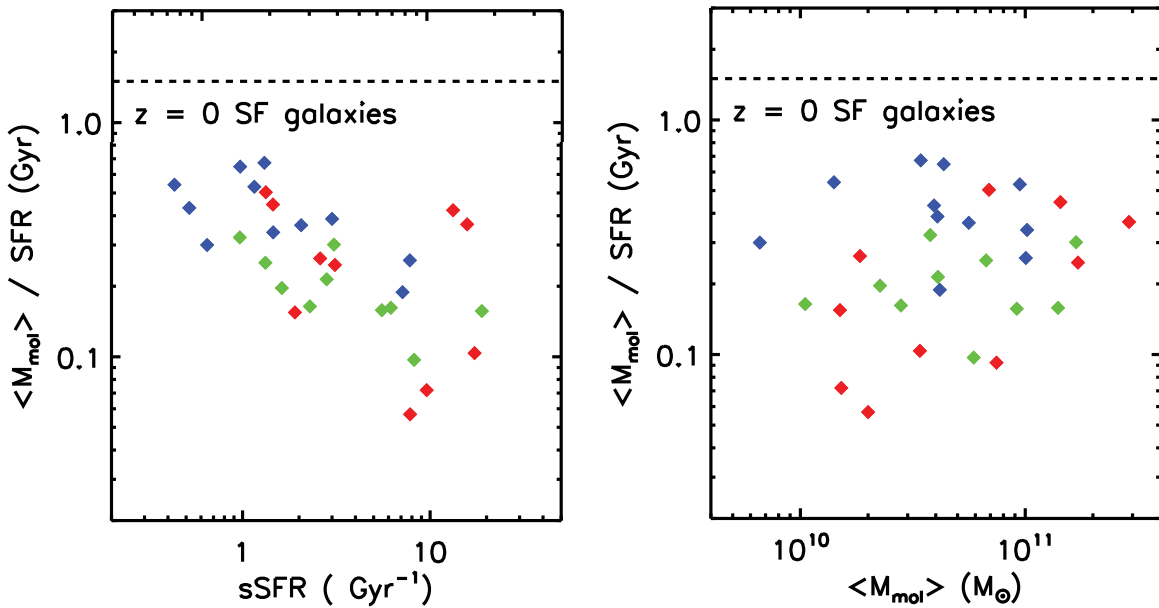


Figure 10. Gas depletion times ( $\tau_{\text{dep}} = M_{\text{mol}}/\text{SFR}$ ) are shown as a function of sSFR and  $M_{\text{mol}}$ .

In fact, variations in the effective dust temperature are probably small on galactic scales since, theoretically, one expects that the mass-weighted  $\langle T_d \rangle_M$  should depend on the  $\sim 1/6$  power of the mean radiation energy density. The observed sub-millimeter fluxes therefore directly probe the total mass of dust and depend only linearly on  $\langle T_d \rangle_M$ , which varies very little. Magnelli et al. (2014) investigated the variations in  $T_D$  derived from SED fits for stacks of galaxies at  $z = 1$  to 2.3 from the MS to a factor of 10 above the MS. The temperatures were found to increase from  $\sim 25$  to 33 K going to sSFR 10 times above the MS. Once again, we emphasize that those  $T_D$  are luminosity-weighted, not mass-weighted, but even so, they do not indicate very large variations. Genzel et al. (2015) have also advocated the use of a variable  $T_D$  to reduce apparent scatter in the relationship between high-J CO lines and the dust continuum; however, much of this scatter is likely due to CO excitation variations which enter from the use of higher-J transitions, and so we do not follow this route.

In practice, it will be difficult or impossible to determine  $\langle T_d \rangle_M$  in most sources since the observed SEDs are not of sufficient accuracy to measure the small secondary peak due to the cold dust on the RJ tail of the SED. Moreover, this peak is unlikely to be discrete since there will be a range of temperatures in the cold component. In the Galaxy, the Planck data show  $\langle T_d \rangle_M = 15\text{--}22$  K (Planck Collaboration 2011b). Recognizing that most of the galaxies with higher SF rates at high redshift are likely to have slightly elevated dust temperatures, we adopt  $\langle T_d \rangle_M = 25$  K for numerical estimates when necessary and might reasonably expect a range of 20–35 K. Since the mass estimates vary as  $T_d^{-1}$ , this range implies less than 25%–30% variation associated with the expected range of global mass-weighted dust temperatures.

Figure 11 shows the  $\Gamma_{\text{RJ}}$  correction factor for dust temperatures of 25 and 35 K. ( $\Gamma_0$  is the value of  $\Gamma$  appropriate to the  $z = 0$ ,  $T_d = 25$  K, and  $\lambda = 850 \mu\text{m}$  used to calibrate  $\alpha_{850 \mu\text{m}}$ ;  $\Gamma_0 = 0.71$  (see Figure 11)).

### A.3. The Dust Sub-millimeter Spectral Index— $\beta$

In order to relate sub-millimeter flux measurements of galaxies at different redshifts (i.e., different rest frame wavelengths) to an empirically constrained mass-light ratio at rest frame  $850 \mu\text{m}$ , one needs to know the spectral index of the RJ dust emission. The overall spectral slope of the rest-frame sub-millimeter dust emission flux density (Equation (5)) is observed to vary as  $S_\nu \propto \nu^\alpha$  with  $\alpha = 3\text{--}4$ . Two powers of  $\nu$  are from the RJ dependence; the remainder is due to the frequency variation in  $\kappa(\nu) \propto \nu^\beta$ . Most theoretical models for the dust have opacity spectral indices of  $\beta = 1.5\text{--}2$  (Draine 2011). Empirical fits to the observed long-wavelength SEDs suggest  $\beta = 1.5\text{--}2$  (Dunne & Eales 2001; Clements et al. 2010) for local galaxies. Probably the best determination at high redshift is that of Chapin et al. (2009), who used their  $\lambda = 1.1$  survey to find  $\langle \beta \rangle = 1.75$  for 29 SMGs with a median  $z = 2.7$ .

Planck has provided a robust Galactic determination of  $\beta$  using 7 sub-millimeter bands (at  $\lambda = 3$  mm to  $100 \mu\text{m}$ ). For the Taurus cloud complex,  $\beta = 1.78 \pm 0.08$  for both atomic and molecular ISM regions (Planck Collaboration 2011b). For the Galaxy, Planck Collaboration (2011a) finds  $\beta = 1.8 \pm 0.1$  with no significant difference between the H I- and H<sub>2</sub>-dominant regions. We therefore adopt  $\beta = 1.8$  when needed in the analysis below.

### A.4. Empirical Calibration from Local Galaxies, Low- $z$ ULIRGs, and $z = 2$ SMGs

In order to empirically calibrate the  $850 \mu\text{m}$  dust opacity per unit gas mass, we make use of galaxy samples for which both the sub-millimeter dust emission and molecular gas masses are well-determined globally for the whole galaxy. Our local sample includes 28 star-forming galaxies from the *Herschel* KINGFISH survey (Dale et al. 2012) and 12 ULIRGs from the *Herschel* VNGS and GOALS surveys (Mentuch Cooper

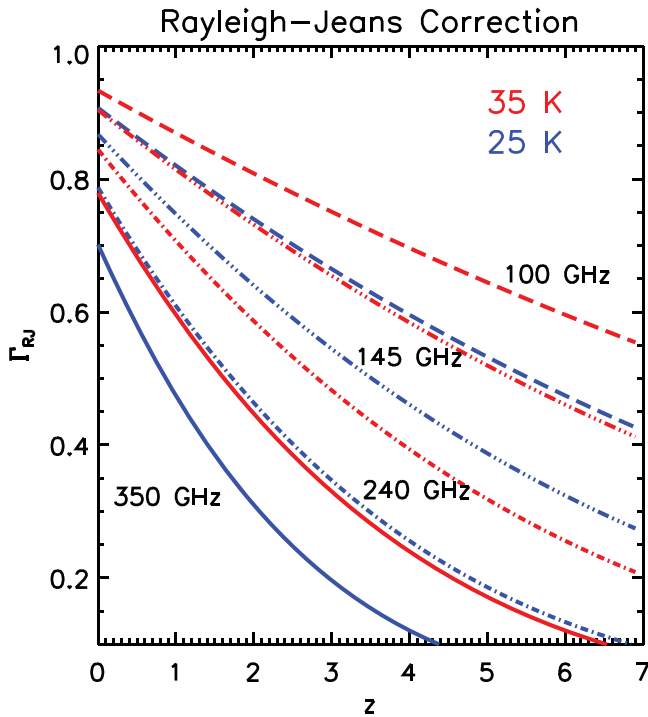


**Figure 11.** RJ correction factor  $\Gamma_{\text{RJ}}$  shown as a function of redshift for four ALMA Bands and dust temperatures of 25 and 35 K.

et al. 2012, J. Chu et al. 2016, in preparation). These have full imaging in the SPIRE 350 and 500  $\mu\text{m}$  bands.<sup>17</sup>

For estimation of the associated gas masses, we have used exclusively CO (1-0) data for which there are also global CO luminosity measures (Sanders et al. 1989, 1991; Young et al. 1995; Solomon et al. 1997) with consistent single-dish calibrations. Although some of these galaxies have millimeter-interferometric imaging, those data often resolve out larger spatial components and therefore often recover less than 50% of the single-dish line fluxes. For the high-redshift SMGs, there are no H I measurements, and so we restrict our empirical calibration entirely to molecular gas masses.

At high redshift, we make use of a sample of 30 SMGs for which there exist good signal-to-noise ratio (S/N) measurements of CO (1-0) from JVLA. For this sample, we use SCUBA 850  $\mu\text{m}$  fluxes since the longer wavelength (compared to SPIRE 500  $\mu\text{m}$ ) is needed to stay on the RJ tail and also because the sources are quite compact. Most of these objects are at  $z < 2.5$ . Based on the high sub-millimeter fluxes, it is clear that many of these SMGs are strongly lensed. This means that the *apparent*  $L_{\nu_{850\mu\text{m}}}$  and  $M_{\text{mol}}$  are large over-estimates of their true values. However, it is reasonable to assume that the magnifications are similar for the dust and the gas emission since they both arise in cold ISM. Thus, the  $L_{\nu_{850\mu\text{m}}}/M_{\text{mol}}$  will provide a consistency check (at high S/N) as to whether or not the relevant combination of the dust-to-gas mass ratio, the dust opacity function, and the mass-weighted  $\langle T_d \rangle_M$  is similar to that in the low- $z$  calibrators.

Our restriction to calibration samples with good CO (1-0) line measurements is very important. Only the CO(1-0) line

<sup>17</sup> These SPIRE data are far superior to the earlier SCUBA imaging for extended galaxies. The ground-based SCUBA observations, taken in beam chopping mode to remove atmospheric background, can cancel extended emission components.

luminosities have been well correlated with virial masses from large Galactic samples of self-gravitating GMCs (Scoville et al. 1987; Solomon et al. 1987). The higher CO transitions have excitation-dependent flux ratios relative to the 1-0 emission luminosities both in Galactic GMCs (Sanders et al. 1993) and in high- $z$  galaxies (Carilli & Walter 2013, see Figure 4). For high-redshift galaxies, this necessarily restricts calibration samples to those observed at high S/N with JVLA or possibly GBT.

The observed SPIRE 500  $\mu\text{m}$  (local galaxies and ULIRGs: Tables 3 and 4) and SCUBA 850  $\mu\text{m}$  (SMGs: Table 5) fluxes were converted to the 850  $\mu\text{m}$  specific luminosity  $L_{\nu(850\mu\text{m})}$  of the assumed 25 K dust using

$$L_{\nu(850\mu\text{m})} = 1.19 \times 10^{27} S_{\nu} [\text{Jy}] \frac{(\nu(850\mu\text{m}))^{3.8}}{\nu_{\text{obs}}(1+z)} \times \frac{(d_L [\text{Mpc}])^2}{1+z} \frac{\Gamma_{\text{RJ}}(25, \nu_{850\mu\text{m}}, 0)}{\Gamma_{\text{RJ}}(25, \nu_{\text{obs}}, z)} \times [\text{erg s}^{-1} \text{Hz}^{-1}]. \quad (10)$$

(The term with ratios of  $\Gamma_{\text{RJ}}$  is necessary since we wish to estimate  $L_{\nu(850\mu\text{m})}$ , which would be associated with 25 K dust producing the same  $L_{\nu}$  at  $\nu = \nu_{\text{obs}} \times (1+z)$  in the observed galaxy rest frame.)

Figure 1 (left) shows the CO(1-0) luminosities for the three samples of galaxies plotted as a function of their specific continuum luminosities at  $\lambda = 850\mu\text{m}$ . All three sets of these very diverse galaxies (normal star-forming, ultraluminous starbursts, and high-redshift starbursts) fall on the same 1:1 line, which provides the empirical basis for using the RJ continuum as a tracer of ISM molecular gas mass. We note that many of these SMGs are likely lensed, but the high magnifications allow the extension of the calibration to high redshift with excellent signal-to-noise ratios. The dust continuum and CO(1-0) emission experiences the same lensing magnifications since the SMGs lie on the same linear correlation as the unmagnified objects at low redshift.

Molecular gas masses were computed from the CO(1-0) integrated fluxes ( $S\Delta\nu$ ) or line luminosities ( $L'_{\text{CO}}$ ) using the relations (Solomon & Vanden Bout 2005; Bolatto et al. 2013)

$$L'_{\text{CO}} [\text{K km s}^{-1} \text{pc}^2] = 3.25 \times 10^7 (S\Delta\nu [\text{Jy km s}^{-1}]) \times (\nu_{\text{rest}} [\text{GHz}])^{-2} (1+z)^{-1} (d_L [\text{Mpc}])^2 \quad (11)$$

$$M_{\text{mol}} [M_{\odot}] = 6.5 L'_{\text{CO}} [\text{K km s}^{-1} \text{pc}^2]. \quad (12)$$

The constant ( $\alpha_{\text{CO}} = 6.5 M_{\odot}/\text{K km s}^{-1} \text{pc}^2$ ) in Equation (9) is based on a standard Galactic conversion factor  $X_{\text{CO}} = 3 \times 10^{20} \text{N}(\text{H}_2) \text{cm}^{-2} (\text{K km s}^{-1})^{-1}$  (see below) and includes a factor of 1.36 to account for the associated mass of heavy elements (mostly He at 8% by number). For the local SF galaxies, the integrated CO (1-0) fluxes were all taken from Young et al. (1995), and so they have consistent calibration and technique for integrating over extended galaxies. (In the course of this work, we found that the molecular gas masses used in the KINGFISH papers (Draine et al. 2007; Dale et al. 2012) are actually based on the same Young et al. (1995) CO survey, even though they reference Kennicutt et al. (2003) for the molecular masses.) Draine et al. (2007) argues for (and used) a higher  $X_{\text{CO}} = 4 \times 10^{20}$ , so their  $\text{H}_2$  masses are larger (they do not explicitly include the He contribution).

**Table 3**  
Low- $z$  Star-forming Galaxies with Global CO(1-0) and *Herschel* SPIRE Luminosities

Galaxy	Distance (Mpc)	$S_{\text{CO}(1-0)}$ (Jy)	$\log L'_{\text{CO}(1-0)}$ (K km s $^{-1}$ pc $^2$ )	$\log M_{\text{mol}}$ ( $M_{\odot}$ )	$S_{\nu 350 \mu\text{m}}$ (Jy)	$S_{\nu 500 \mu\text{m}}$ (Jy)	$S_{\nu 850 \mu\text{m}}$ (Jy)	$L_{\nu 850 \mu\text{m}}$ ( $10^{30}$ cgs)	$L_{\nu 850 \mu\text{m}}/M_{\text{mol}}$ ( $10^{20}$ cgs $M_{\odot}^{-1}$ )
Antennae	21.4	2000	9.35	10.16	14.06	4.69	0.803	0.440	0.30
IC342	3.4	29220	8.92	9.73	247.95	96.90	16.886	0.233	0.44
NGC0628	11.4	2160	8.83	9.65	29.07	12.64	2.185	0.340	0.76
NGC1482	22.0	560	8.82	9.63	6.03	2.10	0.359	0.208	0.48
NGC2146	15.0	2840	9.19	10.01	22.13	7.08	1.220	0.328	0.32
NGC2798	24.7	440	8.82	9.63	2.76	1.03	0.175	0.128	0.30
NGC2841	9.8	1870	8.64	9.45	15.20	6.66	1.153	0.132	0.47
NGC2976	3.6	610	7.27	8.09	11.11	4.55	0.793	0.012	0.98
NGC3184	8.1	1120	8.25	9.07	14.53	6.39	1.109	0.087	0.75
NGC3351	9.3	700	8.17	8.98	13.01	5.05	0.876	0.091	0.95
NGC3521	9.0	4920	8.99	9.80	44.84	18.43	3.194	0.309	0.49
NGC3627	8.9	4660	8.95	9.77	35.72	13.68	2.371	0.225	0.38
NGC3938	14.0	1750	8.92	9.73	9.78	4.12	0.711	0.167	0.31
NGC4254	20.0	3000	9.47	10.28	25.27	8.70	1.493	0.714	0.38
NGC4321	20.0	3340	9.51	10.33	26.50	10.26	1.760	0.842	0.40
NGC4536	25.0	740	9.05	9.86	11.97	5.25	0.897	0.670	0.92
NGC4569	20.0	1500	9.16	9.98	8.94	3.49	0.598	0.286	0.30
NGC4579	20.0	910	8.95	9.76	8.43	3.36	0.577	0.276	0.48
NGC4631	9.0	1740	8.54	9.35	51.77	22.80	3.952	0.383	1.72
NGC4725	17.1	1950	9.14	9.96	15.77	7.53	1.296	0.453	0.50
NGC4736	5.3	2560	8.24	9.06	26.60	11.21	1.950	0.066	0.58
NGC4826	5.6	2170	8.22	9.03	15.58	5.99	1.041	0.039	0.36
NGC5055	8.2	5670	8.97	9.78	60.99	24.80	4.301	0.346	0.57
NGC5194	8.2	9210	9.18	9.99	62.60	21.28	3.691	0.297	0.30
NGC5713	26.6	680	9.07	9.88	6.07	2.18	0.372	0.315	0.41
NGC5866	12.5	250	7.98	8.79	2.98	1.08	0.187	0.035	0.57
NGC6946	5.5	12370	8.96	9.77	103.55	40.66	7.071	0.256	0.43
NGC7331	14.7	4160	9.34	10.15	38.57	15.68	2.702	0.700	0.49

**Note.** CO (1-0) line fluxes from Young et al. (1995); SPIRE 350 and 500  $\mu\text{m}$  fluxes from Dale et al. (2012; except NGC 5194—*Herschel* VNGS data release Wilson et al.) with a multiplicative factor of 0.95 for extended source color correction (see Rémy-Ruyer et al. 2015). The 850  $\mu\text{m}$  fluxes listed in column 8 were extrapolated from the 500  $\mu\text{m}$  fluxes assuming a spectral index of  $\beta = 1.8$  and  $\Gamma_{\text{RJ}}$  appropriate for  $T_d = 25$  K.  $L_{\nu 850 \mu\text{m}}$  was computed from the observed fluxes using Equation (10).

**Table 4**  
ULIRG Galaxies with Global CO(1-0) and *Herschel* SPIRE Luminosities

Galaxy	Distance (Mpc)	$\log L'_{\text{CO}(1-0)}$ (K km s $^{-1}$ pc $^2$ )	$\log M_{\text{mol}}$ ( $M_{\odot}$ )	CO References	$S_{\nu 350 \mu\text{m}}$ (Jy)	$S_{\nu 500 \mu\text{m}}$ (Jy)	$S_{\nu 850 \mu\text{m}}$ (Jy)	$L_{\nu 850 \mu\text{m}}$ ( $10^{30}$ cgs)	$L_{\nu 850 \mu\text{m}}/M_{\text{mol}}$ ( $10^{20}$ cgs $M_{\odot}^{-1}$ )
1ZW107	170.0	9.62	10.44	(1)	0.72	0.20	0.029	1.014	0.37
Arp148	143.0	9.54	10.35	(1)	0.92	0.27	0.040	0.988	0.44
Arp 220	79.0	9.76	10.57	(1), (2)	10.89	3.60	0.584	4.359	1.16
IRASF05189-2	168.0	9.72	10.53	(1)	0.59	0.16	0.023	0.790	0.23
IRASF08572+3	232.0	9.13	9.94	(3), (2)	0.16	0.05	0.007	0.429	0.49
IRASF10565+2	176.0	9.73	10.54	(1), (2)	1.15	0.32	0.047	1.749	0.50
IRASF12112+0	292.0	9.96	10.77	(1)	0.65	0.19	0.024	2.489	0.42
IRASF14348-1	330.0	10.12	10.93	(1)	0.61	0.17	0.022	2.834	0.33
IRASF22491-1	301.0	9.77	10.58	(1)	0.24	0.06	0.008	0.866	0.23
Mrk231	174.0	9.72	10.53	(1), (2)	1.83	0.51	0.076	2.741	0.80
Mrk273	153.0	9.67	10.49	(2), (3)	1.36	0.37	0.055	1.551	0.51

**Note.** CO (1-0) line fluxes from: (1) Sanders et al. 1991), (2) Solomon et al. 1997), and (3) Sanders et al. 1989); SPIRE 350 and 500  $\mu\text{m}$  fluxes from J. Chu et al. (2016, in preparation) for all galaxies except Arp 220 (*Herschel* VNGS data release Wilson et al.).  $L_{\nu 850 \mu\text{m}}$  was computed from the observed fluxes using Equation (10).

We note that Bolatto et al. (2013) have advocated a value of  $X_{\text{CO}} = 2 \times 10^{20} \text{ cm}^{-2} (\text{K km s}^{-1})^{-1}$  based largely on Galactic  $\gamma$ -ray emission analysis. However, this relies on low angular resolution  $\gamma$ -ray (CosB, Egret, CGRAO, and Fermi) and CO (Columbia Survey) data sets, which highly weights gas in the solar neighborhood (mostly H I), rather than the molecular ring

in the inner galaxy; it also does not resolve the distant GMCs. The  $\gamma$ -ray approach also relies on the questionable assumption that the high-energy cosmic rays which produce the  $\gamma$ -rays are approximately constant in the Galactic disk, and that these particles fully penetrate the dense molecular clouds. It is noteworthy that there are also large variations in the  $\gamma$ -ray-

**Table 5**  
SMGs at  $z \sim 2$  with CO(1-0) Data

Galaxy	$z$	Distance (Gpc)	References	$\log L'_{\text{CO}(1-0)}$ ( $\text{K km s}^{-1} \text{pc}^2$ )	$\log M_{\text{mol}}$ ( $M_{\odot}$ )	$S_{\nu}(\lambda_{\mu\text{m}})$ (mJy)	$L_{\nu_{850 \mu\text{m}}}$ ( $10^{30} \text{ cgs}$ )	$L_{\nu_{850 \mu\text{m}}}/M_{\text{mol}}$ ( $10^{20} \text{ cgs } M_{\odot}^{-1}$ )
EROJ164502+4	1.44	10.6	(8)	10.83	11.65	4.89(850)	16.362	0.37
H-ATLASJ0903	2.31	18.9	(1)	11.42	12.24	54.70(880)	214.455	1.24
H-ATLASJ0913	2.63	22.2	(1)	11.40	12.21	36.70(880)	145.710	0.89
H-ATLASJ0918	2.58	21.7	(1)	11.53	12.34	18.80(880)	74.504	0.34
H-ATLASJ1132	2.58	21.7	(1)	11.33	12.14	106.00(500)	179.479	1.30
H-ATLASJ1158	2.19	17.8	(1)	11.26	12.07	107.00(500)	150.507	1.29
H-ATLASJ1336	2.20	17.9	(1)	11.36	12.17	36.80(880)	143.699	0.97
H-ATLASJ1344	2.30	18.9	(1)	11.86	12.67	73.10(880)	286.544	0.61
H-ATLASJ1413	2.48	20.7	(1)	11.65	12.46	33.30(880)	131.429	0.46
HATLASJ08493	2.41	20.0	(11)	10.36	11.17	4.60(870)	17.642	1.19
HATLASJ08493	2.42	20.1	(11)	10.22	11.03	6.90(870)	26.468	2.48
HATLASJ08493	2.41	20.0	(11)	11.21	12.02	19.00(870)	72.855	0.70
HATLASJ08493	2.41	20.0	(11)	11.15	11.96	25.00(870)	95.851	1.05
HLSW-01	2.96	25.6	(2)	11.66	12.48	52.80(880)	212.973	0.71
HXMM01	2.31	19.0	(12)	11.66	12.48	27.00(880)	105.868	0.35
SMMJ02399-01	2.81	24.1	(9)	11.35	12.16	23.00(850)	85.752	0.59
SMMJ04135+10	2.85	24.5	(6)	11.39	12.20	25.00(850)	93.462	0.59
SMMJ04431+02	2.51	21.0	(10)	10.90	11.72	7.20(850)	26.346	0.51
SMMJ123549.4	2.20	17.9	(6)	10.89	11.71	8.30(850)	29.839	0.59
SMMJ123707.2	2.49	20.8	(6)	11.44	12.25	10.70(850)	39.105	0.22
SMMJ14009+02	2.93	25.3	(9)	11.09	11.91	15.60(850)	58.678	0.73
SMMJ14011+02	2.57	21.6	(10)	11.11	11.92	12.30(850)	45.161	0.54
SMMJ163550.9	2.52	21.1	(9)	10.97	11.78	8.40(850)	30.754	0.51
SMMJ163554.2	2.52	21.1	(9)	11.09	11.90	15.90(850)	58.212	0.72
SMMJ163555.2	2.52	21.1	(9)	10.83	11.65	12.50(850)	45.765	1.04
SMMJ163650.4	2.38	19.7	(6)	10.98	11.79	8.20(850)	29.793	0.48
SMMJ163658.1	2.45	20.4	(6)	11.04	11.85	10.70(850)	39.022	0.55
SMMJ2135-010	2.33	19.2	(4)	11.78	12.60	106.00(870)	404.977	1.03
SPT-S053816-	2.79	23.8	(5)	11.64	12.46	125.00(870)	488.049	1.71
SPT-S233227-	2.73	23.2	(5)	11.78	12.59	150.00(870)	583.833	1.49

**Note.** Sub-millimeter and CO (1-0) line fluxes from: (1) Harris et al. 2012), (2) Riechers et al. 2011), (3) Lestrade et al. 2011), (4) Thomson et al. 2015), (5) Aravena et al. 2013), (6) Ivison et al. 2011), (7) Carilli et al. 2011), (8) Greve et al. 2003), (9) Thomson et al. 2012), (10) Harris et al. 2010), (11) Ivison et al. 2013), and (12) Fu et al. 2013).  $L_{\nu_{850 \mu\text{m}}}$  was computed from the observed fluxes using Equation (10).

based  $X_{\text{CO}}$  values between the different analyses and as a function of the Galactic radius (Bolatto et al. 2013). In contrast, extensive GMC surveys (with samples of more than 500 resolved GMCs in the inner Galactic plane, independently measured and analyzed) yielded  $X_{\text{CO}} = 3.6$  and  $3.0 \times 10^{20} \text{ cm}^{-2} (\text{K km s}^{-1})^{-1}$  (respectively, Scoville et al. 1987; Solomon et al. 1987, corrected to  $R_0 = 8.5$  kpc).

We have chosen to use a single conversion factor ( $\alpha_{\text{CO}}$  or  $X_{\text{CO}}$ ) for all of the galaxies. A conversion factor that is several times smaller is often used for ULIRGs and SMGs in analyzing the CO transitions seen from the hot, dense nuclear regions of these merger systems. Similar to the argument we have given above for a uniform  $T_D$ , a smaller value of  $\alpha_{\text{CO}}$  is inappropriate for the globally distributed molecular gas, even though it will sometimes be appropriate for high-resolution observations which isolate the nuclear regions.

In Figure 1, the ratios  $L_{\nu_{850 \mu\text{m}}}/M_{\text{mol}}$  are plotted as a function of  $L_{\nu_{850 \mu\text{m}}}$  for the three samples of galaxies listed in Tables 3–5. The galaxies in all three samples clearly overlap in the luminosity-to-mass ratios and their mean ratios are indeed very similar. The mean of the local star-forming galaxies, ULIRGs, and SMGs is

$$\alpha_{\nu} \equiv \langle L_{\nu_{850 \mu\text{m}}}/M_{\text{mol}} \rangle = 6.7 \pm 1.7 \times 10^{19} \text{ erg s}^{-1} \text{ Hz}^{-1} M_{\odot}^{-1} \quad (13)$$

and we adopt this value in the analysis below.

#### A.5. Planck Measurements for $\text{H I}$ and $\text{H}_2$ in the Galaxy

The Planck measurements of the sub-millimeter emission from the Galaxy provide both very high photometric accuracy and the ability to probe variations in the opacity-to-mass ratio between the atomic and molecular phases, and with Galactic radius. (The latter could possibly provide a probe of metallicity dependence.)

In the Taurus complex, the Planck Collaboration (2011a) obtained resolved observations of the  $\text{H I}$  and  $\text{H}_2$  ISM components with best-fit ratios of  $\tau_{250 \mu\text{m}}/N_{\text{H}} = 1.1 \pm 0.2$  and  $2.32 \pm 0.3 \times 10^{-25} \text{ cm}^2$  for the atomic and molecular phases. The  $\text{H I}$  column densities were derived from the optically thin 21 cm emission with a small correction of 25% for optically thick 21 cm emission. The  $\text{H}_2$  column densities were taken from Pineda et al. (2010), who used NIR extinction measures as a primary measure of molecular gas column densities. (CO column densities were also obtained from a non-LTE radiative transfer analysis but these were not used for the Planck analysis). The mean dust temperature from the Planck observations was 18 K, derived in Taurus, and the mean  $\langle \beta \rangle = 1.8$ . We translate the value given above for  $\tau_{250 \mu\text{m}}/N_{\text{H}}$  in the molecular phase into a specific luminosity per unit mass of

ISM (using  $M_{\text{mol}} = 1.36 M_{\text{H}_2}$  to account to He):

$$\begin{aligned} \frac{L_{\nu_{850 \mu\text{m}}}}{M_{\text{H}_2}} &= [\tau_{250 \mu\text{m}}/N_{\text{H}}] \left( \frac{\nu_{850 \mu\text{m}}}{\nu_{250 \mu\text{m}}} \right)^\beta \frac{4\pi B_\nu(T_d)}{m_{\text{H}}} \\ &= 8.4 \times 10^{19} \text{ erg s}^{-1} \text{ Hz}^{-1} M_\odot^{-1} \\ \alpha_{850 \mu\text{m}} &= \frac{L_{\nu_{850 \mu\text{m}}}}{M_{\text{mol}}} = 6.2 \times 10^{19} \text{ erg s}^{-1} \text{ Hz}^{-1} M_\odot^{-1}. \end{aligned} \quad (14)$$

This value for  $\alpha_{850 \mu\text{m}}$  obtained from the Planck data in Taurus is remarkably similar to that found above (Equation (13)) in the samples of nearby star-forming galaxies, ULIRGs, and  $z \sim 2$  SMGs. Using Planck data from the Galaxy, Planck Collaboration (2011b) found  $\tau_{250 \mu\text{m}}/N_{\text{H}} = 0.92 \pm 0.05 \times 10^{-25} \text{ cm}^2$  near the solar circle. This determination at low angular resolution and covering a large range of galactic latitude is strongly weighted toward the H I phase in the solar neighborhood. Hence, it is not surprising that it agrees better with the value found in Taurus for the atomic gas.

#### A.6. Expected Sub-millimeter Fluxes as a Function of Redshift

Combining Equations (10) and (5), the expected flux density at the observed frequency  $\nu_{\text{obs}}$  is given by

$$\begin{aligned} S_{\nu_{\text{obs}}} &= 0.563 \frac{M_{\text{mol}}}{10^{10} M_\odot} (1+z)^{4.8} \left( \frac{\nu_{\text{obs}}}{\nu_{850 \mu\text{m}}} \right)^{3.8} (d_L [\text{Gpc}])^{-2} \\ &\times \left\{ \frac{\alpha_{850}}{6.7 \times 10^{19}} \right\} \frac{\Gamma_{\text{RJ}}}{\Gamma_0} \text{ mJy} \\ &\text{for } \lambda_{\text{rest}} \gtrsim 250 \mu\text{m}. \end{aligned} \quad (15)$$

We note that the empirical calibration of  $\alpha_{850}$  was obtained from  $z \simeq 0$  galaxies that have a non-negligible RJ departure ( $\Gamma_0 \sim 0.7$ ) which must be normalized out (i.e., the  $y$ -axis intercept in Figure 11). This is the term  $\Gamma_0 = \Gamma_{\text{RJ}}(0, T_d, \nu_{850})$  in the equation above.

The restriction  $\lambda_{\text{rest}} \gtrsim 250 \mu\text{m}$  is intended to ensure that one is on the RJ tail and that the dust is likely to be optically thin. If the dust is extremely cold, then one might need to be more restrictive, and in the case of the most extreme ULIRGs the dust is probably optically thick to even longer wavelengths. Analogous expressions are readily obtained for the other ALMA bands.

Figure 2 shows the expected flux as a function of redshift for the ALMA bands at 100, 145, 240, and 350 GHz (Bands 3, 4, 6, and 7). At low  $z$ , the increasing luminosity distance leads to reduced flux as  $z$  increases. However, above  $z = 1$ , the well-known “negative  $k$ -correction” causes the flux per unit ISM mass to increase at higher  $z$  as one moves up the far-infrared SED toward the peak at  $\lambda \sim 100 \mu\text{m}$ . Figure 2 shows that the 350 GHz flux density plateaus at  $z = 1$  and then decreases above  $z = 2$ . The latter is due to the fact that at higher redshift, the observed frame 350 GHz is approaching the rest-frame far-infrared peak (and no longer on the  $\nu^2$  RJ tail). This is the factor  $\Gamma_{\text{RJ}}$  coming in for 25 K dust.

At redshifts above 2.5, Figure 2 indicates that one needs to shift to a lower frequency band, e.g., 240, 145, or 100 GHz, in order to avoid the large and uncertain  $\Gamma_{\text{RJ}}$  corrections. Since future studies similar to that pursued here will push to higher redshifts, we have included the lower frequency bands in Figures 11 and 2.

Inverting Equation (15), the estimation of masses from observed flux densities can be done using

$$\begin{aligned} M_{\text{mol}} &= 1.78 S_{\nu_{\text{obs}}} [\text{mJy}] (1+z)^{-4.8} \\ &\times \left( \frac{\nu_{850 \mu\text{m}}}{\nu_{\text{obs}}} \right)^{3.8} (d_L [\text{Gpc}])^2 \\ &\times \left\{ \frac{6.7 \times 10^{19}}{\alpha_{850}} \right\} \frac{\Gamma_{\text{RJ}}}{\Gamma_0} 10^{10} M_\odot \\ &\text{for } \lambda_{\text{rest}} > 250 \mu\text{m}. \end{aligned} \quad (16)$$

The restriction  $\lambda_{\text{rest}} \gtrsim 250 \mu\text{m}$  is intended to ensure that one stays on the Rayleigh–Jeans tail.

In the above analysis, we used a single (standard) Galactic conversion factor  $\alpha_{\text{CO}}$  to convert the observed CO(1-0) luminosity to gas mass. As discussed in Solomon & Vanden Bout (2005), low- $z$  studies of ULIRGs have led to the suggestion that the conversion factor could be several times smaller (Downes et al. 1993; Bryant & Scoville 1999). This can arise in the ULIRGs if the gas is concentrated in the nuclear regions (as a result of dissipative galaxy merging) and the molecular emission linewidths can be broadened by the galactic dynamics associated with the stellar mass—not just the self-gravitating gas mass as in individual GMCs in which the standard conversion factor was derived. In addition, the mean gas temperature and density ( $\rho$ ) may be different in the ULIRG nuclei as a result of the intense star formation activity, and  $\alpha_{\text{CO}}$  should vary as  $\langle \rho \rangle^{1/2} / T_k$  (Dickman et al. 1986; Scoville 2012, 2013, Equation (8.5)).

Given the results obtained here, which clearly show a quite similar  $\alpha_{850 \mu\text{m}}$  in all three samples of galaxies, it would appear that there is little basis for using different  $\alpha_{\text{CO}}$  for normal and star bursting galaxies—at least when considering global measurements. For the high- $z$  SMGs, it is not obvious that the lower  $\alpha_{\text{CO}}$  (often used in low- $z$  ULIRGs) is appropriate since it is uncertain that the bulk of the molecular gas in the SMGs is similarly concentrated. Our restriction to CO(1-0) in the above sample was specifically intended to avoid sensitivity to the presence of high excitation gas, and to sample the larger, presumably extended masses of cold gas. Indeed, the ratio of dust emission to gas mass is similar to that obtained in low- $z$  galaxies.

#### A.7. Summary—An Approximately Constant RJ Mass-to-light Ratio

In the preceding sections, we have presented the physical explanation and, more importantly, strong empirical justification for using the long-wavelength RJ dust emission in galaxies as a linear probe of ISM mass. The most substantial determination of the dust RJ spectral slope is that obtained by Planck from observations of the Galaxy (Planck Collaboration 2011a, 2011b), indicating a dust emissivity index  $\beta = 1.8 \pm 0.1$  with no strong evidence of variation in Galactic radius or between atomic and molecular regions. Second, both the Planck data and measurements for nearby local galaxies, including both normal star-forming and star bursting systems, indicate a similar constant of proportionality  $\alpha_{850}$  for the dust emission at rest-frame  $850 \mu\text{m}$  per unit mass of ISM. Finally, we find that for a large sample of SMGs at  $z = 1.4$  to 3, their ratio of rest-frame  $850 \mu\text{m}$  per unit mass of ISM is essentially identical to that obtained for local galaxies. The similarities of these values of  $\alpha_{850}$  argue strongly that for

**Table 6**  
Low- $z$  Galaxy Sample in Band 7

#	R.A. (2000) ( $^{\circ}$ )	decl. (2000) ( $^{\circ}$ )	$z^a$	$S_{\text{tot}}$ (mJy)	$\sigma_{\text{tot}}$ (mJy)	$S_{\text{peak}}$ (mJy)	$\sigma_{\text{pix}}$ (mJy)	S/N <sup>b</sup>	$M_*$ <sup>a</sup> ( $10^{11}M_{\odot}$ )	Log(SFR) <sup>a</sup> ( $M_{\odot} \text{ yr}^{-1}$ )	sSFR /sSFR <sub>MS</sub>	$M_{\text{mol}}$ ( $10^{10}M_{\odot}$ )
890088	149.8157	2.6503	1.02	0.38	0.19	0.71	0.17	4.15	0.28	1.19	0.65	$3.22 \pm 0.78$
846385	149.5421	2.5816	1.01	0.37	0.18	0.62	0.18	2.00	0.39	1.43	1.00	<2.41
405136	150.7642	1.9077	1.02	0.26	0.13	0.33	0.10	2.00	0.28	1.35	0.92	<1.40
471515	149.8180	2.0132	1.04	0.24	0.12	0.37	0.11	2.00	0.40	1.40	0.88	<1.46
257225	149.9700	1.6731	1.01	0.20	0.10	0.29	0.10	2.00	0.32	1.11	0.51	<1.39
354566	149.9792	1.8278	1.19	0.83	0.32	0.36	0.11	2.55	0.38	1.47	0.85	$3.99 \pm 1.57$
737603	150.0182	2.4177	1.12	0.31	0.16	0.51	0.15	2.00	0.52	1.20	0.46	<2.08
787724	149.8601	2.4920	1.19	0.25	0.12	0.58	0.15	3.80	0.52	1.48	0.78	$2.72 \pm 0.72$
543756	150.0946	2.1280	1.22	0.28	0.14	0.62	0.14	4.28	0.60	1.44	0.66	$2.99 \pm 0.70$
805480	150.0256	2.5211	1.03	0.30	0.15	0.46	0.16	2.00	0.79	1.51	0.96	<2.24
687914	149.7395	2.3413	1.01	0.33	0.17	0.63	0.16	3.96	0.38	1.47	1.10	$2.86 \pm 0.72$
711951	149.8388	2.3775	1.21	0.30	0.15	2.63	0.16	16.47	0.39	1.84	1.90	$12.78 \pm 0.78$
800281	150.0747	2.5130	1.26	0.31	0.16	0.47	0.15	2.00	0.39	1.78	1.60	<2.18
873708	150.1164	2.6253	1.02	0.29	0.14	0.57	0.18	2.00	0.39	1.63	1.54	<2.38
599889	150.3524	2.2101	1.23	2.48	0.50	0.45	0.15	5.02	0.99	2.03	2.28	$12.10 \pm 2.41$
671444	150.2712	2.3184	1.16	1.21	0.48	0.63	0.15	2.53	0.85	1.88	1.84	$5.80 \pm 2.29$
918541	149.8367	2.6918	1.01	1.07	0.46	0.64	0.18	2.35	0.54	1.60	1.32	$4.82 \pm 2.05$
984597	150.1099	2.7994	1.09	0.38	0.19	0.50	0.18	2.00	0.44	1.64	1.38	<2.53
802829	149.7721	2.5171	1.14	2.62	0.40	0.61	0.17	6.60	0.72	1.75	1.45	$12.47 \pm 1.89$
806656	150.2180	2.5217	1.20	2.00	0.41	0.60	0.16	4.91	0.74	1.88	1.77	$9.66 \pm 1.97$
842212	150.0628	2.5741	1.01	0.44	0.17	0.66	0.17	3.98	0.95	1.80	1.84	$1.99 \pm 0.50$
483264	150.2705	2.0338	1.20	0.27	0.13	0.32	0.11	2.00	0.41	1.77	1.63	<1.66
541203	149.6961	2.1223	1.37	3.02	0.56	0.55	0.15	5.40	1.28	2.11	2.21	$15.18 \pm 2.81$
914622	150.0537	2.6861	1.03	0.37	0.18	0.57	0.17	2.00	2.88	1.94	2.21	<2.37
983395	150.6615	2.7970	1.18	1.26	0.63	0.73	0.18	2.00	1.05	1.95	2.00	$6.04 \pm 3.02$
985857	150.3477	2.8015	1.25	1.10	0.49	0.54	0.17	3.15	1.39	1.91	1.60	$5.37 \pm 1.70$
422455	149.8490	1.9337	1.24	0.74	0.24	0.28	0.11	3.10	2.12	1.87	1.44	$3.60 \pm 1.16$
434350	150.3446	1.9540	1.24	0.86	0.41	0.34	0.11	2.11	1.86	1.77	1.15	$4.22 \pm 2.00$
505822	149.6633	2.0667	1.24	1.75	0.39	0.43	0.10	4.51	1.66	2.09	2.43	$8.58 \pm 1.90$
340442	150.1541	1.8042	1.11	2.28	1.13	1.04	0.11	2.01	1.59	1.96	2.15	$10.70 \pm 5.32$
868539	149.8634	2.6178	1.32	3.87	0.79	1.81	0.17	4.89	0.35	2.04	2.74	$19.31 \pm 3.95$
288391	150.4103	2.6264	1.15	0.32	0.16	2.24	0.18	12.61	0.28	1.96	3.14	$10.68 \pm 0.85$
960580	149.9191	2.7605	1.16	2.66	0.50	0.58	0.17	5.36	0.35	2.07	3.67	$12.69 \pm 2.37$
409265	149.7843	1.9128	1.16	0.69	0.27	0.33	0.11	2.60	0.39	2.11	3.84	$3.31 \pm 1.27$
351159	150.0908	1.8211	1.00	0.20	0.10	0.35	0.10	2.00	0.35	1.91	3.14	<1.39
601886	149.8117	2.2123	1.22	0.30	0.15	0.50	0.16	2.00	0.95	2.35	4.86	<2.32
237348	149.4016	2.4509	1.19	3.08	0.50	1.85	0.16	6.18	0.76	2.24	4.09	$14.89 \pm 2.41$
781580	149.9086	2.4833	1.25	0.52	0.15	0.56	0.15	3.40	0.75	2.12	2.91	$2.53 \pm 0.74$
134318	150.2174	2.1141	1.13	0.90	0.45	0.80	0.15	2.00	0.44	2.22	4.90	$4.24 \pm 2.12$
560724	150.1236	2.1498	1.17	1.83	0.42	0.41	0.15	4.37	0.83	2.15	3.40	$8.78 \pm 2.01$
585275	150.3987	2.1885	1.04	2.98	0.39	2.02	0.15	7.67	0.78	2.18	4.43	$13.56 \pm 1.77$
969105	150.5307	2.7755	1.36	0.89	0.35	0.65	0.18	2.55	0.96	2.33	3.83	$4.47 \pm 1.75$
831023	150.4179	2.5585	1.21	2.55	0.98	0.54	0.16	3.25	0.71	2.28	4.46	$12.35 \pm 3.80$
6496	149.9741	1.6435	1.04	1.23	0.40	0.47	0.10	3.05	0.76	2.16	4.24	$5.60 \pm 1.84$
418048	150.3503	1.9282	1.20	2.14	0.44	0.46	0.11	4.81	0.83	2.15	3.21	$10.35 \pm 2.15$
108065	150.0087	2.0257	1.19	1.45	0.65	0.35	0.10	2.23	0.76	2.09	2.93	$7.02 \pm 3.14$
269311	149.4324	1.6924	1.26	2.86	0.54	1.30	0.11	5.32	0.61	2.16	3.24	$14.08 \pm 2.65$
160476	149.5986	2.2004	1.20	3.94	0.95	1.05	0.15	4.17	2.24	2.44	5.65	$19.06 \pm 4.57$
872762	150.1296	2.6214	1.41	3.57	1.46	0.96	0.16	2.44	2.31	2.28	2.91	$18.11 \pm 7.42$
916658	150.2231	2.6903	1.30	0.39	0.19	0.52	0.17	2.00	1.24	2.42	5.01	<2.60
811432	150.0425	2.5266	1.18	2.56	0.36	0.77	0.16	4.72	1.85	2.13	2.85	$12.30 \pm 2.61$
485345	150.1895	2.0370	1.18	2.31	0.35	0.75	0.11	6.52	1.12	2.19	3.44	$11.11 \pm 1.70$
370733	150.4130	1.8517	1.20	1.72	0.21	0.35	0.11	8.33	1.26	2.11	2.79	$8.32 \pm 1.00$
627524	149.9813	2.2536	1.36	0.27	0.14	1.28	0.15	8.38	0.22	2.36	6.77	$6.42 \pm 0.77$
344653	150.5036	1.8118	1.16	1.95	0.27	1.16	0.11	7.11	0.36	2.34	6.58	$9.35 \pm 1.31$
504172	149.8325	2.0660	1.15	2.84	0.28	1.72	0.15	10.22	0.66	2.44	7.06	$13.51 \pm 1.32$
9254	150.0120	1.6521	1.30	1.44	0.29	0.69	0.11	6.38	0.42	2.65	10.92	$7.16 \pm 1.12$
570293	150.0981	2.1658	1.20	2.11	0.50	1.46	0.15	9.64	2.06	2.48	6.15	$10.19 \pm 1.06$

**Notes.**

<sup>a</sup> The photometric redshifts and stellar masses of the galaxies are from Ilbert et al. (2013) and the accuracy of those quantities is discussed in detail there. The SFRs are derived from the rest-frame UV continuum and the infrared using *Herschel* PACS and SPIRE data as detailed in Scoville et al. (2013). All of the galaxies have greater than  $10\sigma$  photometry measurements, and so the uncertainties in  $M_*$  and SFR associated with their measurements are always less than 10%. As discussed in Ilbert et al. (2013), the uncertainties in models used to derive the  $M_*$  and SFR from the photometry are larger but generally less than a factor of 2.

<sup>b</sup>  $S/N_{\text{tot}}$  and  $S/N_{\text{peak}}$  are calculated separately and the column S/N lists the larger in absolute magnitude of those two S/Ns. Note that we let the S/N be negative in cases where the flux estimate is negative so that several  $\sigma$  negative flux values do not end up with a positive S/N above the detection thresholds.

**Table 7**  
Mid- $z$  Galaxy Sample in Band 7

#	R.A. (2000) ( $^{\circ}$ )	decl. (2000) ( $^{\circ}$ )	$z^a$	$S_{\text{tot}}$ (mJy)	$\sigma_{\text{tot}}$ (mJy)	$S_{\text{peak}}$ (mJy)	$\sigma_{\text{pix}}$ (mJy)	S/N <sup>b</sup>	$M_*^a$ ( $10^{11}M_{\odot}$ )	Log(SFR) <sup>a</sup> ( $M_{\odot} \text{ yr}^{-1}$ )	sSFR /sSFR <sub>MS</sub>	$M_{\text{mol}}$ ( $10^{10}M_{\odot}$ )
399465	150.4691	1.8996	2.20	0.26	0.13	0.34	0.14	2.00	0.35	1.86	0.69	<2.29
479473	150.0251	2.0288	2.17	0.24	0.12	0.42	0.14	2.00	0.26	1.70	0.56	<2.25
35012	149.9635	1.7615	2.00	0.40	0.15	0.39	0.15	2.55	0.32	1.81	0.78	$2.18 \pm 0.86$
829041	149.7756	2.5571	2.03	1.10	0.24	0.36	0.12	4.58	0.27	1.82	0.83	$5.97 \pm 1.30$
612589	149.9561	2.2301	2.43	0.26	0.13	0.30	0.12	2.00	0.21	1.88	0.73	<1.97
708203	150.7118	2.3724	2.28	0.26	0.13	0.39	0.12	2.00	0.31	1.72	0.49	<1.93
306429	150.1298	1.7536	2.31	1.13	0.52	0.60	0.15	4.11	0.50	1.93	0.66	$6.23 \pm 1.52$
777598	149.9130	2.4806	2.89	0.48	0.20	0.25	0.06	2.43	0.72	2.09	0.72	$6.55 \pm 2.70$
524944	150.0317	2.0987	2.34	1.63	0.49	0.59	0.12	3.32	0.82	2.01	0.68	$8.97 \pm 2.70$
348260	150.2028	1.8191	2.39	1.74	0.37	0.65	0.14	4.55	1.59	2.22	0.96	$9.63 \pm 2.11$
715833	150.5795	2.3850	2.71	0.46	0.20	0.29	0.06	2.29	1.15	2.04	0.59	$6.44 \pm 2.81$
323041	149.8165	1.7798	2.11	1.54	0.47	0.73	0.14	5.18	0.33	2.29	2.08	$8.37 \pm 1.62$
961356	149.6007	2.7629	2.37	0.27	0.14	0.42	0.13	2.00	0.16	2.29	2.34	<2.09
374178	149.7167	1.8609	2.28	0.89	0.12	0.77	0.07	7.10	0.32	2.34	2.01	$13.04 \pm 1.84$
608918	150.1193	2.2241	2.25	1.66	0.33	0.46	0.12	4.99	0.17	1.95	1.14	$9.12 \pm 1.83$
759305	150.3527	2.4511	1.91	0.26	0.13	0.35	0.12	2.00	0.24	2.09	1.82	<1.92
516419	149.7464	2.0845	2.14	0.22	0.11	0.36	0.12	2.00	0.38	2.10	1.25	<1.94
401783	149.9235	1.9038	2.16	3.08	0.50	1.55	0.14	6.16	0.87	2.40	1.94	$16.80 \pm 2.73$
414218	149.9098	1.9234	2.07	1.46	0.03	0.57	0.13	42.61	0.40	2.01	1.04	$7.91 \pm 0.19$
444936	149.7446	1.9724	2.30	1.41	0.44	0.66	0.15	3.23	0.78	2.30	1.37	$7.76 \pm 2.41$
95500	149.8838	1.9812	2.13	2.31	0.60	0.74	0.15	3.83	0.79	2.25	1.41	$12.60 \pm 3.29$
254938	150.3699	1.6707	2.01	0.77	0.24	0.46	0.13	3.43	0.79	2.09	1.11	$4.16 \pm 1.21$
818426	150.7220	2.5419	2.30	0.49	0.14	0.47	0.12	3.42	0.75	2.51	2.26	$2.70 \pm 0.79$
482039	150.1189	2.0321	2.15	0.23	0.12	0.39	0.12	2.00	0.84	2.11	1.00	<1.92
575173	149.9899	2.1741	2.01	1.03	0.50	0.46	0.12	2.05	0.54	2.28	1.91	$5.58 \pm 2.72$
672025	150.0164	2.3210	2.33	2.73	0.47	1.51	0.12	5.77	0.52	2.33	1.60	$15.03 \pm 2.60$
254150	150.0934	2.5073	2.22	3.74	0.49	2.21	0.12	7.58	0.76	2.21	1.21	$20.48 \pm 2.70$
514900	150.4552	2.0835	2.78	1.41	0.25	0.70	0.12	5.75	0.56	2.33	1.33	$7.95 \pm 1.38$
283400	149.6042	1.7164	2.05	4.18	0.02	2.95	0.15	174.99	2.37	2.41	1.96	$22.67 \pm 0.13$
311139	149.7768	1.7610	2.30	1.86	0.54	1.14	0.15	7.85	1.28	2.47	1.87	$10.23 \pm 1.30$
277716	149.4757	2.5882	2.04	2.14	0.78	0.93	0.13	2.73	2.63	2.36	1.72	$11.58 \pm 4.24$
909889	149.6367	2.6824	2.23	0.43	0.16	0.44	0.13	2.77	1.10	2.23	1.18	$2.36 \pm 0.85$
919588	150.1266	2.6961	2.22	4.62	1.22	3.25	0.13	3.79	2.32	2.45	1.82	$25.26 \pm 6.66$
932436	150.3178	2.7165	2.58	4.83	0.47	2.05	0.12	10.21	2.80	2.46	1.43	$26.97 \pm 2.64$
969701	149.5260	2.7769	2.09	1.42	0.30	0.64	0.12	4.75	1.29	2.38	1.82	$7.70 \pm 1.62$
830116	150.5398	2.5586	1.84	2.75	1.24	1.14	0.13	2.22	2.64	2.30	1.87	$14.72 \pm 6.64$
561437	150.5270	2.1541	2.73	4.66	0.34	1.50	0.12	13.84	1.64	2.62	2.18	$26.23 \pm 1.90$
421924	150.3745	1.9364	2.34	1.66	0.55	0.90	0.15	6.01	0.31	2.77	5.19	$9.17 \pm 1.52$
464593	150.3526	2.0048	2.21	2.47	0.58	2.15	0.14	4.23	0.65	2.70	3.94	$13.51 \pm 3.19$
287250	149.6534	1.7231	2.84	3.07	0.60	2.20	0.15	14.97	0.71	2.66	2.67	$17.40 \pm 1.16$
903144	150.4592	2.6714	2.04	1.21	0.41	0.59	0.13	2.98	0.54	2.54	3.31	$6.56 \pm 2.20$
917423	149.9921	2.6934	2.12	2.98	1.20	1.44	0.13	2.49	0.72	2.82	5.47	$16.20 \pm 6.51$
953800	150.1102	2.7516	2.30	8.66	0.65	4.05	0.13	13.35	1.00	2.75	3.75	$47.57 \pm 3.56$
821753	150.2927	2.5466	2.60	1.31	0.52	0.61	0.12	2.53	0.57	2.67	2.89	$7.31 \pm 2.90$
274938	149.9980	2.5782	2.35	1.89	0.34	1.17	0.15	5.59	0.72	2.94	5.85	$10.43 \pm 1.87$
476581	150.3899	2.0247	2.73	1.53	0.30	1.31	0.06	5.08	0.86	2.95	5.05	$21.37 \pm 4.20$
562990	150.1608	2.1547	2.30	2.08	0.33	0.45	0.12	6.40	0.49	2.56	2.81	$11.44 \pm 1.79$
122443	149.6588	2.0720	2.29	5.42	0.56	2.36	0.12	9.62	0.72	2.68	3.34	$29.78 \pm 3.09$
514719	149.5358	2.0825	2.17	0.25	0.13	0.40	0.12	2.00	0.84	2.54	2.65	<1.97
338500	150.2649	1.8029	2.36	9.17	0.67	6.11	0.16	13.79	1.69	2.68	2.78	$50.54 \pm 3.67$
372039	150.4384	1.8561	2.58	9.46	0.61	7.01	0.15	15.60	1.23	2.82	3.54	$52.75 \pm 3.38$
427827	150.3416	1.9456	2.78	3.47	0.29	2.67	0.18	15.08	3.32	2.73	2.65	$19.58 \pm 1.30$
842737	150.6338	2.5783	2.67	8.24	0.73	5.29	0.12	11.23	1.32	2.87	3.92	$46.21 \pm 4.11$
932331	149.6556	2.7162	2.11	7.13	1.08	3.47	0.13	6.63	2.83	2.58	2.66	$38.77 \pm 5.85$
942076	150.1471	2.7315	2.42	14.33	0.39	5.73	0.13	36.79	1.44	2.82	3.70	$79.24 \pm 2.15$
264030	150.7057	2.5404	2.15	4.34	0.69	2.19	0.12	6.26	1.95	2.72	3.68	$23.64 \pm 3.77$
495704	149.9889	2.0533	1.92	5.90	0.61	2.06	0.12	9.61	2.04	2.76	4.98	$31.73 \pm 3.30$
723263	149.8893	2.3964	2.18	5.26	0.61	2.69	0.13	8.56	1.06	2.59	2.85	$28.71 \pm 3.36$
126711	149.6679	2.0874	2.30	11.42	0.59	4.96	0.13	19.47	1.74	2.91	4.94	$62.76 \pm 3.22$
518250	150.1799	2.0886	2.32	5.40	0.31	3.00	0.13	17.62	2.65	2.67	2.71	$29.71 \pm 1.69$
135052	150.4957	2.1162	2.21	4.89	0.67	2.30	0.12	7.29	1.23	2.70	3.44	$26.73 \pm 3.66$
408649	149.6658	1.9139	1.93	3.33	0.49	2.51	0.14	18.62	1.46	2.85	6.26	$17.91 \pm 0.96$
980250	150.0161	2.7924	1.80	7.13	1.20	2.99	0.13	5.96	1.76	2.84	6.98	$37.96 \pm 6.37$

**Table 7**  
(Continued)

#	R.A. (2000) (°)	decl. (2000) (°)	$z^a$	$S_{\text{tot}}$ (mJy)	$\sigma_{\text{tot}}$ (mJy)	$S_{\text{peak}}$ (mJy)	$\sigma_{\text{pix}}$ (mJy)	S/N <sup>b</sup>	$M_*$ <sup>a</sup> ( $10^{11}M_{\odot}$ )	Log(SFR) <sup>a</sup> ( $M_{\odot} \text{ yr}^{-1}$ )	sSFR /sSFR <sub>MS</sub>	$M_{\text{mol}}$ ( $10^{10}M_{\odot}$ )
815012	150.6034	2.5366	2.10	5.38	0.74	3.55	0.13	7.32	1.57	3.10	9.36	$29.24 \pm 4.00$

**Notes.**

<sup>a</sup> The photometric redshifts and stellar masses of the galaxies are from Ilbert et al. (2013) and the accuracy of those quantities is discussed in detail there. The SFRs are derived from the rest-frame UV continuum and the infrared using *Herschel* PACS and SPIRE data as detailed in Scoville et al. (2013). All of the galaxies have greater than  $10\sigma$  photometry measurements, and so the uncertainties in  $M_*$  and SFR associated with their measurements are always less than 10%. As discussed in Ilbert et al. (2013) the uncertainties in models used to derive the  $M_*$  and SFR from the photometry are larger but generally less than a factor of 2.

<sup>b</sup> S/N<sub>tot</sub> and S/N<sub>peak</sub> are calculated separately and the column S/N lists the larger in absolute magnitude of those two S/Ns. Note that we let the S/N be negative in cases where the flux estimate is negative so that several  $\sigma$  negative flux values do not end up with a positive S/N above the detection thresholds.

**Table 8**  
High- $z$  Galaxy Sample in Band 6

#	R.A. (2000) (°)	decl. (2000) (°)	$z^a$	$S_{\text{tot}}$ (mJy)	$\sigma_{\text{tot}}$ (mJy)	$S_{\text{peak}}$ (mJy)	$\sigma_{\text{pix}}$ (mJy)	S/N <sup>b</sup>	$M_*$ <sup>a</sup> ( $10^{11}M_{\odot}$ )	Log(SFR) <sup>a</sup> ( $M_{\odot} \text{ yr}^{-1}$ )	sSFR /sSFR <sub>MS</sub>	$M_{\text{mol}}$ ( $10^{10}M_{\odot}$ )
566428	150.0300	2.1627	5.89	0.14	0.07	0.22	0.07	2.00	0.25	1.74	0.46	<2.51
457406	150.3921	1.9937	4.00	0.16	0.08	0.19	0.06	2.10	0.26	1.83	0.56	$2.03 \pm 0.97$
286380	150.0598	1.7217	4.35	0.12	0.06	0.31	0.07	4.69	0.31	1.94	0.67	$3.77 \pm 0.80$
477614	150.3071	2.0261	4.30	0.13	0.07	0.18	0.07	2.00	0.45	2.07	0.79	<2.41
249399	150.1373	2.4902	4.16	0.09	0.05	0.18	0.06	2.00	0.56	1.90	0.50	<2.16
735699	150.6181	2.4158	4.04	0.55	0.11	0.20	0.06	3.54	1.03	2.14	0.75	$6.90 \pm 1.95$
608706	150.5920	2.2251	4.85	0.11	0.05	0.21	0.07	2.00	0.16	2.35	2.37	<2.41
972851	149.9827	2.7821	4.82	0.10	0.05	0.14	0.06	2.00	0.24	2.30	1.72	<2.07
284164	150.5189	2.6097	4.21	0.13	0.07	0.14	0.06	2.00	0.33	2.48	2.27	<2.23
386988	150.1413	1.8805	4.71	0.30	0.11	0.17	0.06	2.89	0.18	2.04	1.08	$3.71 \pm 1.28$
256965	150.3371	1.6746	4.59	0.39	0.17	0.26	0.06	4.21	0.18	2.32	2.09	$4.81 \pm 1.14$
41128	149.3435	1.7836	5.59	0.13	0.06	0.16	0.06	2.00	0.45	2.55	2.35	<2.32
582526	149.8712	2.1871	4.55	0.12	0.06	0.21	0.06	2.00	3.66	2.48	1.48	<2.34
331108	150.4637	2.7859	4.49	1.98	0.35	1.12	0.06	19.54	1.02	2.53	1.85	$24.34 \pm 1.25$
901851	150.4011	2.6707	4.14	0.27	0.07	0.23	0.06	3.77	0.11	2.40	3.38	$3.33 \pm 0.88$
302769	150.0692	1.7477	4.33	0.58	0.15	0.27	0.06	3.88	0.12	2.46	3.65	$7.12 \pm 1.84$
307139	150.1546	1.7550	4.30	0.46	0.05	0.21	0.06	3.35	0.36	2.66	3.30	$5.72 \pm 1.71$
881017	150.4657	2.6361	3.54	2.24	0.40	1.33	0.06	23.27	0.50	2.90	5.10	$28.95 \pm 1.24$
468591	150.5352	2.0115	4.13	1.43	0.15	0.84	0.07	9.54	1.06	2.73	2.95	$17.85 \pm 1.87$
536066	150.4204	2.1177	3.96	1.34	0.11	0.99	0.07	11.91	2.48	2.89	3.86	$16.87 \pm 1.42$
564267	150.2446	2.1597	4.00	1.39	0.35	1.02	0.07	15.65	3.16	2.89	3.82	$17.46 \pm 1.12$
480666	149.4872	2.0303	4.18	0.60	0.14	0.24	0.07	3.60	0.14	2.91	9.40	$7.45 \pm 2.07$
315797	149.9304	1.7687	4.64	3.84	0.35	2.49	0.06	39.14	0.84	3.05	6.35	$47.03 \pm 1.20$

**Notes.**

<sup>a</sup> The photometric redshifts and stellar masses of the galaxies are from Ilbert et al. (2013) and the accuracy of those quantities is discussed in detail there. The SFRs are derived from the rest-frame UV continuum and the infrared using *Herschel* PACS and SPIRE data as detailed in Scoville et al. (2013). All of the galaxies have greater than  $10\sigma$  photometry measurements so the uncertainties in  $M_*$  and SFR associated with their measurements are always less than 10%. As discussed in Ilbert et al. (2013) the uncertainties in models used to derive the  $M_*$  and SFR from the photometry are larger but generally less than a factor of 2.

<sup>b</sup> S/N<sub>tot</sub> and S/N<sub>peak</sub> are calculated separately and the column S/N lists the larger in absolute magnitude of those two S/Ns. Note that we let the S/N be negative in cases where the flux estimate is negative so that several  $\sigma$  negative flux values do not end up with a positive S/N above the detection thresholds.

global ISM masses, the dust emissivity at long wavelengths, the dust-to-gas mass ratio, and the mass-weighted dust temperatures vary little.

The sub-millimeter flux to dust mass ratio is expected to vary linearly with dust temperature. In practice, the overall range of  $T_d$  for the bulk of the mass of the ISM is very small, since it requires very large increases in radiative heating to increase the dust temperatures ( $T_d$  varies approximately as the 1/5–1/6 power of the radiation energy density). As noted above, the extensive surveys of local galaxies using *Herschel* find a range of  $T_d \sim 15$ –30 K (Dunne et al. 2011; Dale et al. 2012; Auld et al. 2013). Where we have needed to specify a dust temperature (e.g., for the  $R$ – $J$  correction) we have adopted

25 K, so we expect the uncertainties in the derived masses averaged on galaxy scales will be less than  $\sim 25\%$ .

These calibrations include normal to star bursting systems and low to moderate redshifts; they lay a solid foundation for using measurements of the RJ dust emission to probe galactic ISM masses. ALMA enables this technique for high-redshift surveys, providing high sensitivity and the requisite angular resolution to avoid source confusion.

**A.8. Cautions**

It is important to recognize that even for those objects detected in SPIRE, the SPIRE data cannot be used to reliably estimate ISM masses (along the lines as is done here) for the

$z = 1$  and 2 samples. For those redshifts, the SPIRE data will be probing near the rest-frame far-infrared luminosity peak—*not safely on the RJ tail and not necessarily optically thin*. The longest wavelength channel ( $500\ \mu\text{m}$  or  $600\ \text{GHz}$ ) will be probing the rest-frame  $170\ \mu\text{m}$  for  $z = 2$  for such measurements, so there will be substantial uncertainty in the mass estimate, depending on the assumed value of the dust temperature (see Figure 11). (In addition, the  $500\ \mu\text{m}$  SPIRE data has relatively high source confusion on account of the large beam size.)

Often, the far-infrared SEDs are analyzed by fitting either modified black body curves or libraries of dust SEDs to the observed SEDs (e.g., Draine et al. 2007; da Cunha & Charlot 2011; Magdis et al. 2012a, 2012b). In essentially all of the instances, the intrinsic SEDs used for fitting are taken to be optically thin. They thus do not include the attenuation expected near the far-infrared peak associated with optically thick dust, instead attributing the drop at short wavelengths to a lack of high temperature grains. The  $T_D$  determined in these cases is not even the luminosity-weighted  $T_D$  of all of the dust, just the dust above  $\tau \sim 1$ .

Fitting the observed SED to derive an effective dust temperature is not a reliable approach—near the far-infrared peak, the temperature characterizing the emission is “luminosity-weighted” (i.e., grains undergoing strong radiative heating) rather than mass-weighted. Hence, the derived  $T_d$  will not reflect the temperature appropriate to the bulk of the ISM mass. Or, put another way, the flux measured near the peak is simply a measure of luminosity, not mass. At high redshifts, the large SPIRE beam at  $500\ \mu\text{m}$  results in severe source confusion at the expected flux levels; hence, reliable flux measurements for individual galaxies are difficult. At  $z > 2$ , ALMA resolution and sensitivity are required and one must observe at  $\nu \leq 350\ \text{GHz}$  to be on the RJ tail of the dust emission.

One might be concerned that some of the correlation between the SPIRE  $500\ \mu\text{m}$  continuum and the CO(1-0) in our local galaxy samples was due to emission lines contributing substantially to the continuum flux in the SPIRE data. However, scaling the CO(1-0) fluxes (given in the above tables) to the frequencies covered in the  $500\ \mu\text{m}$  filter (having width  $\lambda/\Delta\lambda = 2.5$ ) indicates that the CO lines will contribute less than  $10^{-3}$  of the total continuum flux. At rest wavelengths longer than 2 mm, line contamination becomes an issue since the line fluxes decrease less rapidly than  $\lambda^{-2}$  while the dust continuum decreases as  $\sim\lambda^{-3.8}$ . In fact, the Planck imaging of nearby molecular clouds shows positive excess residuals at a level of 10% relative to the dust emission in the 100 GHz band (Planck Collaboration 2011a, attributed to CO(1-0) emission).

Finally, we reiterate the caution that the calibration samples are intentionally restricted to objects with high stellar mass ( $M_{\text{stellar}} > 5 \times 10^{10} M_{\odot}$ ); thus, we are not probing lower metallicity systems where the dust-to-gas abundance ratio is likely to drop or where there could be significant molecular gas without CO (see Bolatto et al. 2013). A similar calibration at lower metallicities will be more difficult given the lower CO and continuum fluxes and, in fact, at very low metallicities it is quite likely that this technique will not be as robust.

## APPENDIX B INDIVIDUAL GALAXIES AND THEIR FLUXES

In Tables 6–8, we list the individual flux measurements, and galaxy properties are summarized for all 145 galaxies in our

survey. The objects are taken from the COSMOS survey field (Scoville et al. 2007) and the galaxy properties are from the latest photometric redshift catalog (Ilbert et al. 2013). This catalog has high accuracy photometric redshifts based on very deep 34-band photometry, including near-infrared photometry from the Ultra-Vista survey. See Ilbert et al. (2013) and Laigle (2016) for discussions of the accuracy of the redshifts and the stellar masses of the galaxies. The SFRs in Column 9 are from Lee et al. (2015) where there are two-band *Herschel* detections and from Laigle (2016) using the UV continuum and optical/UV continuum SEDs.

The galaxy ID # given in column 1 is taken from the most up-to-date COSMOS photometric redshift catalog (Laigle 2016). Columns 5 and 7 in each table list the integrated and peak flux measurements for apertures of up to  $2''.5$  (Low- $z$  and Mid- $z$ ) and  $2''$  (High- $z$ ) radius centered on the galaxy position. The aperture sizes are intended to include most of a galactic disk ( $\sim 10\ \text{kpc}$ ). The noise estimate in both cases is from the measured dispersion in the integrated and peak flux measurements obtained for 100 displaced off-center apertures of the same size in each individual image. The signal-to-noise ratio given in Column 7 is the better of those obtained from the integrated or peak flux measurement; it is the ratio of the signal in Columns 5 and 7 to the measured noise given in Columns 6 and 8. Columns 10–12 give the galaxy stellar mass, SFR, and sSFR (relative to the MS at the same redshift and  $M_{\text{stellar}}$  with the MS taken from Lee et al. (2015)). In the last column, the derived ISM molecular mass is given. Limits on the masses are at 2 and  $3.6\sigma$ , depending on whether the better S/N (column 9) was obtained for the integrated or peak flux measurement. The detection thresholds of 2 and  $3.6\sigma$  are chosen such that the chance of a spurious detection across the entirety of each sample is less than  $\sim 10\%$  (based on the measured noise in each individual image).

## REFERENCES

- Álvarez-Márquez, A., Burgarella, D., Buat, V., Heinis, S., & Pep/Hermes/Cosmos Teams 2015, in Proc. of the XI Scientific Meeting of the Spanish Meeting of the Spanish Astronomical Society, Highlights of Spanish Astrophysics VIII, ed. A. J. Cenarro et al., 142
- Aravena, M., Murphy, E. J., Aguirre, J. E., et al. 2013, *MNRAS*, 433, 498
- Auld, R., Bianchi, S., Smith, M. W. L., et al. 2013, *MNRAS*, 428, 1880
- Béthermin, M., Daddi, E., Magdis, G., et al. 2012, *ApJL*, 757, L23
- Béthermin, M., Daddi, E., Magdis, G., et al. 2015, *A&A*, 573, A113
- Bolatto, A. D., Wolfire, M., & Leroy, A. K. 2013, *ARA&A*, 51, 207
- Bothwell, M. S., Smail, I., Chapman, S. C., et al. 2013, *MNRAS*, 429, 3047
- Bryant, P. M., & Scoville, N. Z. 1999, *AJ*, 117, 2632
- Carilli, C. L., & Walter, F. 2013, *ARA&A*, 51, 105
- Carilli, C. L., Hodge, J., Walter, F., et al. 2011, *ApJL*, 739, L33
- Casey, C. M. 2012, *MNRAS*, 425, 3094
- Casey, C. M., Chapman, S. C., Neri, R., et al. 2011, *MNRAS*, 415, 2723
- Chapin, E. L., Pope, A., Scott, D., et al. 2009, *MNRAS*, 398, 1793
- Clements, D. L., Dunne, L., & Eales, S. 2010, *MNRAS*, 403, 274
- Coppin, K. E. S., Smail, I., Alexander, D. M., et al. 2009, *MNRAS*, 395, 1905
- da Cunha, E., & Charlot, S. 2011, MAGPHYS: Multi-wavelength Analysis of Galaxy Physical Properties, Astrophysics Source Code Library, ascl:1106.010
- Daddi, E., Bournaud, F., Walter, F., et al. 2010, *ApJ*, 713, 686
- Dale, D. A., Aniano, G., Engelbracht, C. W., et al. 2012, *ApJ*, 745, 95
- Dickman, R. L., Snell, R. L., & Schloerb, F. P. 1986, *ApJ*, 309, 326
- Downes, D., Solomon, P. M., & Radford, S. J. E. 1993, *ApJL*, 414, L13
- Draine, B. T. 2011, Physics of the Interstellar and Intergalactic Medium (Princeton, NJ: Princeton Univ. Press)
- Draine, B. T., Dale, D. A., Bendo, G., et al. 2007, *ApJ*, 663, 866
- Dunne, L., & Eales, S. A. 2001, *MNRAS*, 327, 697
- Dunne, L., Gomez, H. L., da Cunha, E., et al. 2011, *MNRAS*, 417, 1510
- Eales, S., Smith, M. W. L., Auld, R., et al. 2012, *ApJ*, 761, 168

- Elbaz, D., Dickinson, M., Hwang, H. S., et al. 2011, *A&A*, **533**, A119
- Fu, H., Cooray, A., Feruglio, C., et al. 2013, *Natur*, **498**, 338
- Genzel, R., Tacconi, L. J., Gracia-Carpio, J., et al. 2010, *MNRAS*, **407**, 2091
- Genzel, R., Tacconi, L. J., Lutz, D., et al. 2015, *ApJ*, **800**, 20
- Greve, T. R., Ivison, R. J., & Papadopoulos, P. P. 2003, *ApJ*, **599**, 839
- Harris, A. I., Baker, A. J., Frayer, D. T., et al. 2012, *ApJ*, **752**, 152
- Harris, A. I., Baker, A. J., Zonak, S. G., et al. 2010, *ApJ*, **723**, 1139
- Harvey, P. M., Fallscheer, C., Ginsburg, A., et al. 2013, *ApJ*, **764**, 133
- Hopkins, A. M., & Beacom, J. F. 2006, *ApJ*, **651**, 142
- Ilbert, O., McCracken, H. J., Le Fèvre, O., et al. 2013, *A&A*, **556**, A55
- Ivison, R. J., Papadopoulos, P. P., Smail, I., et al. 2011, *MNRAS*, **412**, 1913
- Ivison, R. J., Swinbank, A. M., Smail, I., et al. 2013, *ApJ*, **772**, 137
- Karim, A., Schinnerer, E., Martínez-Sansigre, A., et al. 2011, *ApJ*, **730**, 61
- Kennicutt, R. C., Jr., Armus, L., Bendo, G., et al. 2003, *PASP*, **115**, 928
- Laigle, C., McCracken, Ilbert, H. J., et al. 2016, *A&A*, submitted
- Lee, N., Sanders, D. B., Casey, C. M., et al. 2015, *ApJ*, **801**, 80
- Leroy, A. K., Walter, F., Sandstrom, K., et al. 2013, *AJ*, **146**, 19
- Lestrade, J.-F., Carilli, C. L., Thanjavur, K., et al. 2011, *ApJL*, **739**, L30
- Magdis, G. E., Daddi, E., Béthermin, M., et al. 2012a, *ApJ*, **760**, 6
- Magdis, G. E., Daddi, E., Sargent, M., et al. 2012b, *ApJL*, **758**, L9
- Magnelli, B., Lutz, D., Saintonge, A., et al. 2014, *A&A*, **561**, A86
- McCracken, H. J., Milvang-Jensen, B., Dunlop, J., et al. 2012, *A&A*, **544**, A156
- McMillan, P. J. 2011, *MNRAS*, **414**, 2446
- Mentuch Cooper, E., Wilson, C. D., Foyle, K., et al. 2012, *ApJ*, **755**, 165
- Motte, F., Zavagno, A., Bontemps, S., et al. 2010, *A&A*, **518**, L77
- Noeske, K. G., Weiner, B. J., Faber, S. M., et al. 2007, *ApJL*, **660**, L43
- Pineda, J. L., Goldsmith, P. F., Chapman, N., et al. 2010, *ApJ*, **721**, 686
- Planck Collaboration 2011a, *A&A*, **536**, A21
- Planck Collaboration 2011b, *A&A*, **536**, A25
- Rémy-Ruyer, A., Madden, S. C., Galliano, F., et al. 2015, *A&A*, **582**, A121
- Riechers, D. A., Hodge, J., Walter, F., Carilli, C. L., & Bertoldi, F. 2011, *ApJL*, **739**, L31
- Rivera-Ingraham, A., Martin, P. G., Polychroni, D., et al. 2015, *ApJ*, **809**, 81
- Rodighiero, G., Daddi, E., Baronchelli, I., et al. 2011, *ApJL*, **739**, L40
- Sanders, D. B., Scoville, N. Z., & Soifer, B. T. 1991, *ApJ*, **370**, 158
- Sanders, D. B., Scoville, N. Z., Tilanus, R. P. J., Wang, Z., & Zhou, S. 1993, in AIP Conf. Ser. 278, Back to the Galaxy, ed. S. S. Holt & F. Verter (Melville, NY: AIP), 311
- Sanders, D. B., Scoville, N. Z., Zensus, A., et al. 1989, *A&A*, **213**, L5
- Santini, P., Maiolino, R., Magnelli, B., et al. 2014, *A&A*, **562**, A30
- Sargent, M. T., Béthermin, M., Daddi, E., & Elbaz, D. 2012, *ApJL*, **747**, L31
- Sargent, M. T., Daddi, E., Béthermin, M., et al. 2014, *ApJ*, **793**, 19
- Schreiber, C., Pannella, M., Elbaz, D., et al. 2015, *A&A*, **575**, A74
- Scoville, N., Aussel, H., Brusa, M., et al. 2007, *ApJS*, **172**, 1
- Scoville, N., Aussel, H., Sheth, K., et al. 2014, *ApJ*, **783**, 84
- Scoville, N., Arnouts, S., Aussel, H., et al. 2013, *ApJS*, **206**, 3
- Scoville, N., Sheth, K., Walter, F., et al. 2015, *ApJ*, **800**, 70
- Scoville, N. Z. 2012, arXiv:1210.6990
- Scoville, N. Z. 2013, in Secular Evolution of Galaxies, ed. J. Falcón-Barroso & J. H. Knapen (Cambridge: Cambridge Univ. Press), 491
- Scoville, N. Z., Yun, M. S., Sanders, D. B., Clemens, D. P., & Waller, W. H. 1987, *ApJS*, **63**, 821
- Silverman, J. D., Daddi, E., Rodighiero, G., et al. 2015, *ApJL*, **812**, L23
- Solomon, P. M., Downes, D., Radford, S. J. E., & Barrett, J. W. 1997, *ApJ*, **478**, 144
- Solomon, P. M., Rivolo, A. R., Barrett, J., & Yahil, A. 1987, *ApJ*, **319**, 730
- Solomon, P. M., & Vanden Bout, P. A. 2005, *ARA&A*, **43**, 677
- Speagle, J. S., Steinhardt, C. L., Capak, P. L., & Silverman, J. D. 2014, *ApJS*, **214**, 15
- Steinhardt, C. L., Speagle, J. S., Capak, P., et al. 2014, *ApJL*, **791**, L25
- Tacconi, L. J., Genzel, R., Neri, R., et al. 2010, *Natur*, **463**, 781
- Tacconi, L. J., Neri, R., Genzel, R., et al. 2013, *ApJ*, **768**, 74
- Thomson, A. P., Ivison, R. J., Owen, F. N., et al. 2015, *MNRAS*, **448**, 1874
- Thomson, A. P., Ivison, R. J., Smail, I., et al. 2012, *MNRAS*, **425**, 2203
- Toft, S., Smolčić, V., Magnelli, B., et al. 2014, *ApJ*, **782**, 68
- Whitaker, K. E., van Dokkum, P. G., Brammer, G., & Franx, M. 2012, *ApJL*, **754**, L29
- Wilson, C. D., Rangwala, N., Glenn, J., et al. 2014, *ApJL*, **789**, L36
- Young, J. S., & Scoville, N. Z. 1991, *ARA&A*, **29**, 581
- Young, J. S., Xie, S., Tacconi, L., et al. 1995, *ApJS*, **98**, 219



ERRATUM: “ISM MASSES AND THE STAR FORMATION LAW AT  $Z = 1$  TO 6 ALMA OBSERVATIONS OF DUST CONTINUUM IN 145 GALAXIES IN THE COSMOS SURVEY FIELD” (2016, *ApJ*, 820, 83)

N. SCOVILLE<sup>1</sup>, K. SHETH<sup>2</sup>, H. AUSSEL<sup>3</sup>, P. VANDEN BOUT<sup>4</sup>, P. CAPAK<sup>5</sup>, A. BONGIORNO<sup>6</sup>, C. M. CASEY<sup>7</sup>, L. MURCHIKOVA<sup>1</sup>, J. KODA<sup>8</sup>, J. ÁLVAREZ-MÁRQUEZ<sup>9</sup>, N. LEE<sup>10</sup>, C. LAIGLE<sup>11</sup>, H. J. MCCrackEN<sup>11</sup>, O. ILBERT<sup>9</sup>, A. POPE<sup>12</sup>, D. SANDERS<sup>10</sup>, J. CHU<sup>10</sup>, S. TOFT<sup>13</sup>, R. J. IVISON<sup>14,15</sup>, AND S. MANOHAR<sup>1</sup>

<sup>1</sup> California Institute of Technology, MC 249-17, 1200 East California Boulevard, Pasadena, CA 91125

<sup>2</sup> North American ALMA Science Center, National Radio Astronomy Observatory, 520 Edgemont Road, Charlottesville, VA 22901, USA

<sup>3</sup> AIM Unité Mixte de Recherche CEA CNRS, Université Paris VII UMR n158, Paris, France

<sup>4</sup> National Radio Astronomy Observatory, 520 Edgemont Road, Charlottesville, VA 22901, USA

<sup>5</sup> Spitzer Science Center, MS 314-6, California Institute of Technology, Pasadena, CA 91125

<sup>6</sup> INAF—Osservatorio Astronomico di Roma, Via di Frascati 33, I-00040 Monteporzio Catone, Rome, Italy

<sup>7</sup> Department of Astronomy, The University of Texas at Austin, 2515 Speedway Blvd Stop C1400, Austin, TX 78712

<sup>8</sup> Department of Physics and Astronomy, SUNY Stony Brook, Stony Brook, NY 11794-3800, USA

<sup>9</sup> Laboratoire d’Astrophysique de Marseille LAM, Université d’Aix-Marseille & CNRS, UMR7326, 38 rue F. Joliot-Curie, F-13388 Marseille Cedex 13, France

<sup>10</sup> Institute for Astronomy, 2680 Woodlawn Dr., University of Hawaii, Honolulu, Hawaii, 96822

<sup>11</sup> CNRS, UMR 7095, Institut d’Astrophysique de Paris, F-75014, Paris, France

<sup>12</sup> Department of Astronomy, University of Massachusetts, Amherst, MA 01003

<sup>13</sup> AD(Dark Cosmology) Centre, Niels Bohr Institute, University of Copenhagen, Juliana Mariesvej 30, DK-2100 Copenhagen, Denmark

<sup>14</sup> Institute for Astronomy, University of Edinburgh, Blackford Hill, Edinburgh EH9 3HJ, UK

<sup>15</sup> ESO, Karl-Schwarzschild-Strasse 2, D-85748 Garching, Germany

Received 2016 April 23; accepted 2016 April 27; published 2016 June 13

1.

Equation (16) had a typographic error with the ratios of  $\Gamma$ ’s inverted. The correct equation should read as:

$$M_{\text{mol}} = 1.78 S_{\nu_{\text{obs}}} [\text{mJy}] (1 + z)^{-4.8} \left( \frac{\nu_{850 \mu\text{m}}}{\nu_{\text{obs}}} \right)^{3.8} (d_L [\text{Gpc}])^2 \\ \times \left\{ \frac{6.7 \times 10^{19}}{\alpha_{850}} \right\} \frac{\Gamma_0}{\Gamma_{RJ}} 10^{10} M_{\odot}.$$

This equation was not used in any of the calculations of  $M_{\text{mol}}$  in the paper and therefore none of the results are affected. The equation was put in the final version of the paper as an aid for others who would want to calculate masses. We were alerted to the problem by Mihwah Han to whom we are grateful.